Numerical and Experimental Investigation of High-Frequency Thermoacoustic Instabilities in a Jet-Stabilized Burner

Andreas Fiolitakis,* Michael Pries,† Oliver Lammel,‡ and Trupti Kathrotia§
DLR, German Aerospace Center, 70569 Stuttgart, Germany

https://doi.org/10.2514/1.B39885

In this work, we investigate high-frequency thermoacoustic instabilities in a jet-stabilized gas turbine burner by means of large-eddy simulation (LES). This burner is operated at 8 bar pressure with a mixture of hydrogen and natural gas. Experimental data for the pressure oscillations in the combustion chamber are provided here to validate the simulations. The LES is conducted using a splitting scheme for solving the equations for compressible, reactive flows. To model the filtered chemical source terms in LES, two different models (namely an assumed probability density function (APDF) model and a thickened flame (TF) model) are used. Time-resolved computational data are analyzed using multiresolution proper orthogonal decomposition. It is found that mainly three longitudinal modes and one mixed transverse–longitudinal mode cause the high-frequency instabilities in the combustor. Computed frequencies of these modes agree excellently with measured frequencies. Amplitudes of the modes are best reproduced by the use of the TF model. Further analysis of the computational data obtained with the TF model reveals that heat release fluctuations caused by periodic distortion of the flame geometry and by fluctuations in equivalence ratio play an important role in the thermoacoustic feedback.

Nomenclature

A	=	area, m^2
a	=	temporal coefficient of multiresolution proper orthogonal decomposition
C_W	=	wall-adapting local eddy-viscosity model constant
C_M	=	concentration of collision partner, mol/m^3
C_α	=	concentration of species α, mol/m^3
c	=	isentropic speed of sound, m/s
c_v	=	specific heat capacity at constant volume, $J/(kg \cdot K)$
D_α	=	diffusion coefficient of species α, m^2/s
D_{JC}	=	diameter of jet carrier, m
E	=	specific total energy, J/kg
e	=	specific internal energy, J/kg
f	=	frequency, Hz
h	=	specific enthalpy, J/kg
$h^0_{f,\alpha}$	=	formation enthalpy of species α, J/kg
I	=	frequency band, Hz
$\mathfrak{I}$	=	indicator function of heat release zone
j	=	diffusive mass flux, $kg/(m^2 \cdot s)$
j_t	=	subgrid-scale mass flux, $kg/(m^2 \cdot s)$
k_{kb}	=	rate constant of backward reaction k (units are in mol, m, s)
k_{kf}	=	rate constant of forward reaction k (units are in mol, m, s)
k_t	=	subgrid-scale kinetic energy, m^2/s^2
$L_1 \ldots L_{5+\alpha}$	=	amplitudes of characteristic waves
l	=	length scale, m
M	=	molecular weight, kg/mol
Ma	=	Mach number
N	=	length of time series
N_s	=	number of species
N_r	=	number of reactions
Pr_t	=	subgrid-scale Prandtl number
p	=	pressure, Pa
Q	=	global heat release, W
q	=	diffusive heat flux, $J/(m^2 \cdot s)$
q_t	=	subgrid-scale heat flux, $J/(m^2 \cdot s)$
$\mathfrak{q}$	=	heat release, W/m^3
R_m	=	universal gas constant, $J/(mol \cdot K)$
S	=	chemical source term, $kg/(m^3 \cdot s)$
Sc_t	=	subgrid-scale Schmidt number
St_{JC}	=	Strouhal number of jet carrier
$\mathfrak{S}$	=	sensor function of heat release
s	=	specific entropy, $J/(kg \cdot K)$
$\mathfrak{s}$	=	strain rate tensor, 1/s
T	=	temperature, K
t	=	time, s
U_{JC}	=	velocity scale in jet carrier, m/s
u	=	flow velocity, m/s
u_{ac}	=	acoustic velocity, m/s
u_n	=	normal flow velocity, m/s
$u_{t,1}, u_{t,2}$	=	tangential flow velocities, m/s
V	=	volume, m^3
w_{kb}	=	backward reaction rate of reaction k, $mol/(m^3 \cdot s)$
w_{kf}	=	forward reaction rate of reaction k, $mol/(m^3 \cdot s)$
x	=	spatial coordinate, m
Y_α	=	mass fraction of species α
δ_{ij}	=	Kronecker delta
$\varepsilon_{\mathfrak{S}}$	=	minimum threshold of sensor function
ζ	=	arbitrary variable
λ	=	thermal conductivity, $W/(m \cdot K)$
μ	=	dynamic viscosity, $kg/(m \cdot s)$
μ_t	=	subgrid-scale viscosity, $kg/(m \cdot s)$
ν_M	=	exponent for third-body reaction
$\nu_{\alpha k}$	=	stoichiometric coefficient of species α in reaction k
$\nu^b_{\alpha k}$	=	backward stoichiometric coefficient of species α in reaction k
$\nu^f_{\alpha k}$	=	forward stoichiometric coefficient of species α in reaction k

Presented as Paper 2024-0794 at the AIAA SciTech 2024 Forum, Orlando, FL, January 8–12, 2024; received 8 November 2024; accepted for publication 18 August 2025; published online 3 October 2025.

*Research Scientist, Institute of Combustion Technology, Computer Simulation Department, Baden-Württemberg; andreas.fiolitakis@dlr.de (Corresponding Author).

†Research Scientist, Institute of Combustion Technology, Computer Simulation Department, Baden-Württemberg.

‡Head of Department, Institute of Combustion Technology, Department of Combustor Systems and Diagnostics, Baden-Württemberg.

§Research Scientist, Institute of Combustion Technology, Department of Chemical Kinetics and Analytics, Baden-Württemberg.

ρ	=	density, kg/m^3
ρ_0	=	reference density, kg/m^3
$\sigma_2 \ldots \sigma_{5+\alpha}$	=	model parameters of characteristic waves
τ	=	viscous stress tensor, N/m^2
τ_t	=	subgrid-scale stress tensor, N/m^2
ϕ	=	spatial multiresolution proper orthogonal decomposition mode

Subscripts

CC	=	combustion chamber
CD	=	computational domain
i, j, l	=	spatial index
k	=	summation index
RZ	=	reaction zone
trgt	=	target
α	=	species index
0	=	reference value

Superscripts

T	=	transpose
$'$	=	fluctuation over time average
$\bar{}$	=	filtered quantity
$\tilde{}$	=	Favre-filtered quantity

I. Introduction

THE occurrence of thermoacoustic instabilities is a serious problem in technical combustion systems. These types of instabilities are typically caused by a positive feedback loop between acoustic pressure waves propagating within a combustion device and the unsteady heat release in the combustion chamber. If fluctuations of heat release happen to be "in phase" with pressure oscillations, acoustic energy builds up in the combustion system, and oscillations of pressure as well as velocity can attain high amplitudes. Such high-amplitude oscillations have a detrimental effect on the operation of combustion systems, as they result in enhanced thermal and mechanical loads on the walls of the combustor and even flashback, leading ultimately to premature material fatigue and mechanical failure of the technical components [1]. High-frequency pressure oscillations (i.e., frequencies above 1000 Hz [2]) appear to be exceptionally harmful, as they can cause high-frequency vibrations in the mechanical structure of the combustion system, resulting in a rapid fatigue of the material. Examples of such destructive instabilities are reported in [3,4] for stationary gas turbines, but also the "screech" phenomenon in aeroengines [5,6] and transverse instabilities in rocket engines [7,8] fall in the category of such high-frequency instabilities (HFI). To prevent the occurrence of HFI, model-based understanding of the phenomena involved is of paramount importance. Among different modeling approaches of varying complexity, compressible large-eddy simulation (LES) has emerged as an essential tool for studying combustion instabilities numerically [9]. The LES approach is already used extensively for the computation of thermoacoustic instabilities. Reviews on this topic with emphasis on gas turbine combustion are given in [2,9], and in particular for rocket engine combustion, numerous LES studies exist on self-excited high-frequency oscillations [10–29]. By comparison, fewer studies [30–41] address, to our knowledge, explicitly the computation of self-excited HFI in gas turbine combustors.

The present work is concerned with HFI in a jet-stabilized gas turbine burner. Such burners offer high fuel flexibility and are, therefore, used in modern gas turbines that operate with different fuels, such as blends of hydrogen and natural gas [42]. Advances in the understanding of the mechanisms leading to HFI in such burner systems are, therefore, of great technical importance. However, there are, to our best knowledge, only a few LES investigations available that address HFI in this kind of burner system [37,38,40]. Among these, only [37,40] investigate real burner geometries at elevated pressure. In [37], mainly transverse and mixed transverse–longitudinal modes at 5460 and 6897 Hz are found for pressure oscillations in the combustion chamber, as well as a weaker longitudinal mode at 2586 Hz. Compared to that, a higher frequency is reported in [40] for a radial mode at 10,900 Hz, which is found along with a mixed transverse–longitudinal mode at 5200 Hz. It is observed in [40] that a second burner stage consisting of six nozzles in a jet in a crossflow arrangement changes the dominant oscillation mode from a mixed transverse–longitudinal mode to a radial mode depending on the geometrical shape of these nozzles. However, a verification of the numerical results in [37,40] by a comparison to experimental data, in particular for frequency and amplitude of the pressure oscillations, is lacking. Such a verification is reported in [38], but only for an experiment under atmospheric conditions with a simplified burner geometry featuring a single nozzle. The aim of this work is, therefore, to close this gap by LES investigations of a technically relevant burner experiment where a burner consisting of multiple nozzles is operated at elevated pressure, and where experimental data for HFI are provided in terms of frequency and amplitude of the pressure oscillations.

For this purpose, we resume investigations on HFI for the jet-stabilized burner presented in [37]. Compared to [37], an operating point at a higher pressure is considered here. Also, for the first time, experimental data for pressure are provided for this particular burner configuration along with data for OH* chemiluminescence. These experimental data are used to validate the LES. In addition, the numerical and the modeling approaches are drastically improved compared to [37] as outlined in Sec. III. In particular, closure models for turbulence chemistry interaction are taken into account, which is not the case in [37], where the chemical source term is evaluated based on laminar chemistry. Furthermore, a numerical scheme is used, which ensures monotone solutions.

The main goal of the present work is to provide data on HFI by means of compressible LES in order to elucidate the mechanisms that affect flame stabilization and to investigate the processes leading to heat release oscillations and, subsequently, to HFI. The modes involved in HFI of this burner are of particular interest in this investigation. For this purpose, the computational data obtained in this work are analyzed using multiresolution proper orthogonal decomposition (MRPOD). Modal analysis methods such as proper orthogonal decomposition (POD) [43,44] and dynamic mode decomposition (DMD) [45,46] are used widely in fluid mechanics to analyze complex numerical and experimental data sets. The main objective of mode analysis based on POD and DMD is to reduce the dimensionality and the degrees of freedom by extracting important modes [47,48]. To this end, POD decomposes the data set into modes that capture most of the energy content, whereas DMD extracts the modes from a linear approximation of the dynamic processes in a data set [47]. To perform mode analysis on LES data of HFI, POD and DMD have already been applied extensively in previous work. Examples involve [31], where POD is used, and [17,23,25,29,34,35,49], where DMD is utilized (an exception is [37], where the mode analysis is based on a selective fast-Fourier-filtering approach). A direct comparison of POD versus DMD of LES data is reported in [50]. The MRPOD approach, which is used here instead of POD and DMD, is motivated by the fact that conventional POD identifies spatial modes solely by their energy content. Conventional POD may therefore miss modes that are important to the dynamics of a variable but at the same time have a relatively low energy content. The MRPOD of [51,52] overcomes this problem by incorporating a multiresolution analysis (MRA) on the basis of wavelets (i.e., the cross-correlation matrix of a variable is decomposed using wavelets before computing the POD). In this way, a unique frequency band of a variable is considered in the spectral domain. Compared to DMD, MRPOD offers the distinct advantage that it resolves closely packed frequency components and captures nonperiodic fluctuations, as well as intermittencies [51,52]. Therefore, MRPOD is used in this work to conduct mode analysis of simulation results. Results of the present MRPOD analysis are summarized in Sec. V, where the thermoacoustic feedback loop in this burner is also investigated in detail.

II. Test Case

A detailed description of the burner, which is the subject of the present investigation, is given in [37]. The burner is a 12-nozzle, jet-stabilized gas turbine burner [53] where high-velocity jets of fuel are mixed with air in jet carriers before they enter the combustion chamber (cf. Fig. 1). The gas mixture discharges with high momentum from the jet carriers into the combustion chamber, where it causes exhaust gas recirculation, which aids flame stabilization. In the present study, the burner is fueled with a mixture of hydrogen and natural gas (the mass fractions of hydrogen and natural gas are 22% and 78%, respectively) at a global equivalence ratio of 0.625 (the air and fuel mass flows amount to 505.88 and 15.74 g/s). The combustion chamber (which has a hexagonal shape [54]) is equipped with quartz-glass windows for optical access. The whole burner is mounted into the high-pressure test rig HBK-S of the DLR Institute of Combustion Technology, where experiments at 8 bar pressure are performed. Details on this test rig are given in [55–58]. The pressure oscillations in the combustion chamber are recorded during the operation of the burner by using Kistler dynamic pressure sensors in order to provide validation data for LES. Compared to the pressure measurements presented earlier in [59], we improve the accuracy of the data by taking into account that the pressure sensor is not flush-mounted in the wall. Instead it is connected by a short probe of 9 mm length and 4 mm diameter to the combustion chamber. The transfer function of this probe in terms of magnitude and phase is shown in Fig. 2. An attenuation of the pressure signal is observed for frequencies between 2390 and 5410 Hz. With the help of this transfer function, the pressure signal is corrected. A segment of the corrected pressure signal is given in Fig. 3. Compared to the raw signal, the corrected signal shows a larger amplitude.

To provide an impression of the average flame shape and position in the experiment, an image of OH* chemiluminescence is given in Fig. 4. The image is taken such that four nozzles are visible, as indicated on the left side of Fig. 4. Due to the camera position, the OH* chemiluminescence of the flames at nozzles one and two overlaps the OH* chemiluminescence of the flames at nozzles three and four. It is clear from the OH* chemiluminescence at nozzles one and two that on average the flames anchor at the exit of the jet carriers. The flames are short and compact; i.e., the flame length appears to be of the order of a few diameters of the jet carrier (the jet carrier diameter is $D_{\mathrm{JC}} = 12$ mm, an indication of this length scale is given in the contour plot in Fig. 4). From this perspective, which is not perpendicular to the flames, a precise quantification of the flame length is not possible.

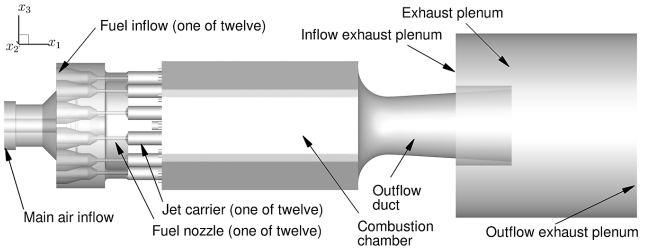

Fig. 1 Solution domain for the LES of the jet-stabilized gas turbine burner.

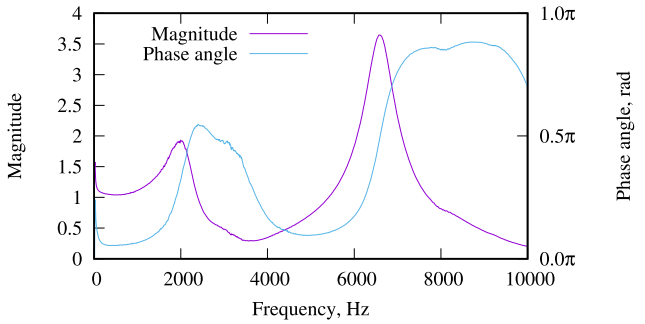

Fig. 2 Magnitude and phase of transfer function of pressure probe.

III. Modeling Approach

A. Filtered Equations

In this work, we are interested in solving numerically the Favre-filtered balance equations for mass, momentum, and energy along with the Favre-filtered transport equations of species mass fractions. These equations are given by

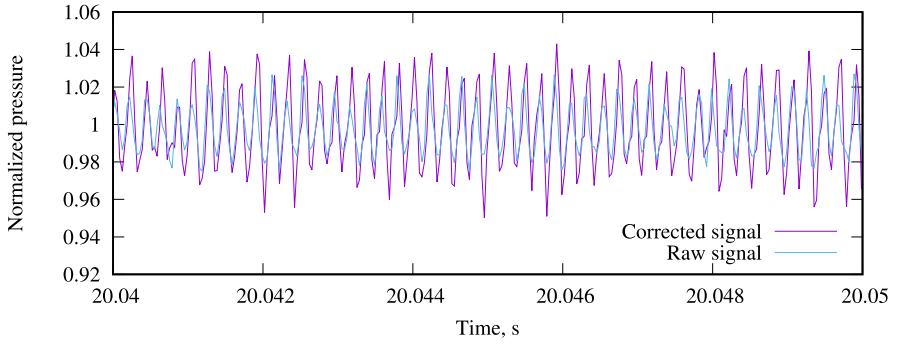

Fig. 3 Normalized measured pressure. The raw signal recorded by the pressure sensor and the corrected signal are given.

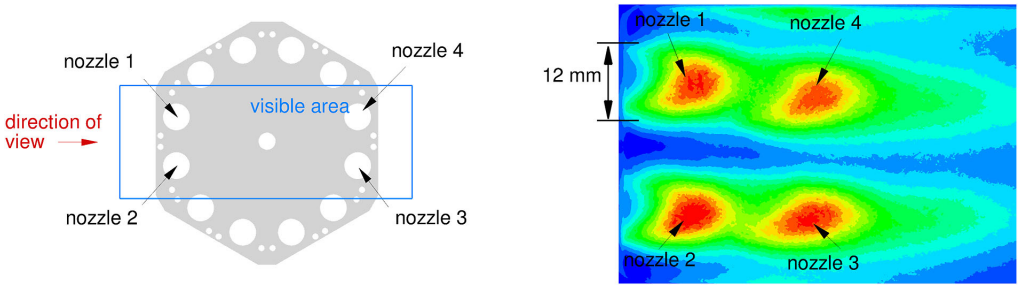

Fig. 4 Side view of OH* chemiluminescence in the combustion chamber during the experiment.

$$\frac{\partial \bar{\rho}}{\partial t} + \frac{\partial \bar{\rho}\tilde{u}_i}{\partial x_i} = 0 \tag{1}$$

$$\frac{\partial \bar{\rho}\tilde{u}_j}{\partial t} + \frac{\partial \bar{\rho}\tilde{u}_i\tilde{u}_j}{\partial x_i} = -\frac{\partial \bar{p}}{\partial x_j} + \frac{\partial(\bar{\tau}_{ij} - \tau_{t,ij})}{\partial x_i} \tag{2}$$

$$\frac{\partial \bar{\rho}\tilde{E}}{\partial t} + \frac{\partial}{\partial x_i}\left(\bar{\rho}\tilde{u}_i\left(\tilde{E} + \frac{\bar{p}}{\bar{\rho}}\right)\right) = \frac{\partial \tilde{u}_j(\bar{\tau}_{ij} - \tau_{t,ij})}{\partial x_i} - \frac{\partial(\bar{q}_i + q_{t,i})}{\partial x_i} \tag{3}$$

$$\frac{\partial \bar{\rho}\tilde{Y}_\alpha}{\partial t} + \frac{\partial \bar{\rho}\tilde{u}_i\tilde{Y}_\alpha}{\partial x_i} = -\frac{\partial(\bar{j}_{i\alpha} + j_{t,i\alpha})}{\partial x_i} + \bar{S}_\alpha \tag{4}$$

Here, t is the time, x_i the spatial coordinate, ρ the density, p the pressure, u_j the velocity vector, Y_α the mass fraction of the species α (there are a total of $N_s - 1$ linearly independent species, where N_s is the total number of species), and E the specific total energy. Note that τ_{ij} is the viscous stress tensor, q_i is the vector of the diffusive heat flux, and $j_{i\alpha}$ and S_α are the diffusive mass flux vector and chemical source term of the species α, respectively. The Favre-filtered specific total energy is given by

$$\tilde{E} = \tilde{e} + \frac{1}{2}\sum_{j=1}^{3}\tilde{u}_j^2 + k_t \tag{5}$$

where e is the specific internal energy and k_t is the subgrid-scale kinetic energy. The operator $\bar{\bullet}$ in the above equations denotes a filtered value. A Favre-filtered value $\tilde{\bullet}$ is defined in terms of filtered quantities as $\tilde{\bullet} = \overline{(\rho\bullet)}/\bar{\rho}$. It is assumed that the fluid is a mixture of thermally perfect gases and that the equation of state is given by the ideal gas law. The Favre-filtered internal energy of the mixture is expressed as

$$\tilde{e} = \sum_{\alpha=1}^{N_s}\tilde{Y}_\alpha\tilde{e}_\alpha \tag{6}$$

where e_α is the internal energy of species α. For a thermally perfect gas, the specific heat capacity at constant volume of a species α (defined as $c_{v,\alpha}$) depends on temperature T only. Hence, the Favre-filtered specific internal energy of a species α is modeled as

$$\tilde{e}_\alpha \approx e_\alpha(\tilde{T}) = h^0_{f,\alpha} + \int_{T_0}^{\tilde{T}} c_{v,\alpha}(T)\,\mathrm{d}T \tag{7}$$

$h^0_{f,\alpha}$ is the formation enthalpy of species α and T_0 the reference temperature. The temperature dependence of $c_{v,\alpha}$ is given by the polynomial representation of NASA [60]. The equation of state is written in terms of filtered variables as

$$\bar{p} = \bar{\rho}R_m\tilde{T}\sum_{\alpha=1}^{N_s}\frac{\tilde{Y}_\alpha}{M_\alpha} \tag{8}$$

where M_α denotes the molecular weight of species α and R_m the universal gas constant. The filtering operation of the balance and transport equations leads to the subgrid-scale stress tensor $\tau_{t,ij}$, the subgrid-scale heat flux $q_{t,i}$, and subgrid-scale species mass flux $j_{t,i\alpha}$. Models for these quantities and for the filtered chemical source term are outlined in Secs. III.C and III.E, respectively. The modeling of the molecular transport phenomena is outlined in Sec. III.D.

B. Numerical Method

To solve Eqs. (1–4) we use the "implicit characteristic splitting–weighted average flux" (ICS-WAF) [61] scheme, which is available in the DLR in-house code ThetaCOM (this scheme is an extension of the "implicit characteristic splitting" (ICS) scheme given in [62]). The ICS-WAF scheme is a two-step splitting scheme that consists of an advective step followed by an acoustic step. The equations of the advective step read

$$\frac{\partial \bar{\rho}}{\partial t} + \frac{\partial \bar{\rho}\tilde{u}_i}{\partial x_i} - \bar{\rho}\frac{\partial \tilde{u}_i}{\partial x_i} = 0 \tag{9}$$

$$\frac{\partial \bar{\rho}\tilde{u}_j}{\partial t} + \frac{\partial \bar{\rho}\tilde{u}_i\tilde{u}_j}{\partial x_i} - \bar{\rho}\tilde{u}_j\frac{\partial \tilde{u}_i}{\partial x_i} = \frac{\partial(\bar{\tau}_{ij} - \tau_{t,ij})}{\partial x_i} \tag{10}$$

$$\frac{\partial \bar{\rho}\tilde{E}}{\partial t} + \frac{\partial \bar{\rho}\tilde{u}_i\tilde{E}}{\partial x_i} - \bar{\rho}\tilde{E}\frac{\partial \tilde{u}_i}{\partial x_i} = \frac{\partial \tilde{u}_j(\bar{\tau}_{ij} - \tau_{t,ij})}{\partial x_i} - \frac{\partial(\bar{q}_i + q_{t,i})}{\partial x_i} \tag{11}$$

$$\frac{\partial \bar{\rho}\tilde{Y}_\alpha}{\partial t} + \frac{\partial \bar{\rho}\tilde{u}_i\tilde{Y}_\alpha}{\partial x_i} - \bar{\rho}\tilde{Y}_\alpha\frac{\partial \tilde{u}_i}{\partial x_i} = -\frac{\partial(\bar{j}_{i\alpha} + j_{t,i\alpha})}{\partial x_i} + \bar{S}_\alpha \tag{12}$$

The equations of the acoustic step of the ICS-WAF scheme are expressed as

$$\frac{\partial \bar{p}}{\partial t} + \bar{\rho}\bar{c}^2\frac{\partial \tilde{u}_i}{\partial x_i} = 0 \tag{13}$$

$$\frac{\partial \tilde{u}_j}{\partial t} + \frac{1}{\bar{\rho}}\frac{\partial \bar{p}}{\partial x_j} = 0 \tag{14}$$

$$\frac{\partial \bar{s}}{\partial t} = 0 \tag{15}$$

$$\frac{\partial \tilde{Y}_\alpha}{\partial t} = 0 \tag{16}$$

where c denotes the isentropic speed of sound. Note that the specific entropy s and the composition Y_α remain constant over time during the acoustic step, but they may vary in space. Compared to the ICS scheme (where a pressure correction equation is solved in the acoustic step [62]), the ICS-WAF scheme solves the hyperbolic equations (13) and (14) directly under the constraints imposed by Eqs. (15) and (16). The advantage of this approach is that the monotonicity of the solution is ensured [61].

The ICS-WAF scheme has been introduced recently as a novel method for computing the mildly compressible flows. Details on the scheme's accuracy and applicability to fluid mechanical problems are summarized in [61]. The scheme is of second-order accuracy in space and time as shown in [61]. Its stability is also proven in [61] by a von Neumann stability analysis for a linear, hyperbolic model problem. Due to its novelty, the scheme is extensively verified for fluid mechanical problems in [61]. This involves inviscid flows (i.e., Riemann problems, including rarefaction waves and mild shocks, propagating acoustic waves, as well as standing pressure waves) and viscous flows (i.e., lid-driven cavities for different Reynolds numbers, laminar boundary-layer flows for Mach numbers between 0.1 and 0.9, Taylor Green vortex for Mach numbers between 0.001 and 0.1, and LES of complex flow). The correct convergence rate of the ICS-WAF scheme into the incompressible limit in terms of Mach number is also verified in [61].

In order to perform LES of the jet-stabilized burner experiment described in Sec. II, the domain shown in Fig. 1 is discretized with an unstructured grid. On this primary grid, a median-dual grid is created for ThetaCOM, which consists of about 10 million control volumes. The highest mesh resolution is found in the jet carriers and the combustion chamber, where the edge length of the primary grid ranges between 0.25 and 0.5 mm. In addition to this coarse grid, a fine grid with 36 million control volumes is also used in one LES in order to study the grid dependency of the solution. In this fine grid, the size of control volumes is reduced by a factor of two in order to achieve twice the grid resolution compared to the coarse grid. This refinement is applied to the area in the jet carriers, in the fuel nozzles, and in the region of flame stabilization at the exit of the jet carriers. The computational time step is 0.1 μs (this corresponds

to a maximum Courant–Friedrichs–Lewy number of about 0.55 and 1 on the coarse and fine grid, respectively, based on the Favre-filtered flow velocity).

Depending on the closure model for the filtered chemical source term, the LES involves 29 or 31 variables. To reduce computational cost for the LES on the fine mesh, we start this LES after the exponential growth phase of the combustion instability is over. These initial values are obtained from LES on the coarse mesh by interpolating the LES solution from the coarse grid onto the fine grid. With this approach, one single LES requires a computing time of about 8 million core-hours on both meshes. 2560 cores and 8192 cores of AMD EPYC 7702 processors (64 cores per CPU and 2 GHz CPU frequency) are used for the computations on the coarse mesh and the fine mesh, respectively. A single run requires about 3 months of wall time on the coarse mesh and about 2 months on the fine mesh.

C. Subgrid-Scale Flux Models

To close the system of equations presented in Sec. III.B, models for the subgrid-scale stress tensor and the subgrid-scale heat and species mass fluxes are required. For the former, we use the wall-adapting local eddy-viscosity (WALE) approach of [63] with a WALE constant of $C_W = 0.1$. The anisotropic part of the subgrid-scale stress tensor reads

$$\tau_{t,ij} - \frac{\delta_{ij}}{3}\sum_{l=1}^{3}\tau_{t,ll} = -2\mu_t\left(\tilde{\mathbb{s}}_{ij} - \frac{\delta_{ij}}{3}\sum_{l=1}^{3}\tilde{\mathbb{s}}_{ll}\right) \tag{17}$$

where $\tilde{\mathbb{s}}_{ij} = 1/2(\partial\tilde{u}_i/\partial x_j + \partial\tilde{u}_j/\partial x_i)$ is the Favre-filtered strain rate tensor, δ_{ij} the Kronecker delta [64], and μ_t the subgrid-scale viscosity, which is given in [63]. The isotropic part of the subgrid-scale stress tensor is neglected for low-Mach-number compressible flows, as discussed in [65]. The subgrid-scale species mass fluxes and energy flux are closed using gradient diffusion approaches [64].

$$j_{t,i\alpha} = -\frac{\mu_t}{Sc_t}\frac{\partial\tilde{Y}_\alpha}{\partial x_i} \tag{18}$$

$$q_{t,i} = -\frac{\mu_t}{Pr_t}\frac{\partial\tilde{h}}{\partial x_i} \tag{19}$$

where the velocity triple correlation is neglected in the energy flux [66]. Sc_t and Pr_t are the subgrid-scale Schmidt and Prandtl numbers, respectively. Note that $\tilde{h} = \tilde{e} + \bar{p}/\bar{\rho}$ is the Favre-filtered specific enthalpy.

D. Molecular Transport Models

The viscous stress tensor is given in terms of the Favre-filtered strain rate tensor as

$$\tau_{ij} = 2\mu\left(\tilde{\mathbb{s}}_{ij} - \frac{\delta_{ij}}{3}\sum_{l=1}^{3}\tilde{\mathbb{s}}_{ll}\right) \tag{20}$$

where μ is the dynamic viscosity. For the diffusive species mass flux, a simplified Fickian approach is employed:

$$j_{i\alpha} = -\bar{\rho}\bar{D}_\alpha\frac{\partial\tilde{Y}_\alpha}{\partial x_i} \tag{21}$$

Individual species diffusivities D_α are used. The diffusive heat flux reads

$$q_{t,i} = -\bar{\lambda}\frac{\partial\tilde{T}}{\partial x_i} + \sum_{\alpha=1}^{N_s}\tilde{h}_\alpha j_{i\alpha} \tag{22}$$

where $\tilde{h}_\alpha = \tilde{e}_\alpha + R_m\tilde{T}/M_\alpha$ is the specific enthalpy of species α, and λ is the thermal conductivity of the mixture. The thermal conductivity and the molecular viscosity of the gas are computed as mixture-averaged values by using filtered variables. Likewise, the molecular viscosity is also computed based on filtered variables.

E. Chemical Source Term Closure

The constitutive equation for the chemical source term reads

$$S_\alpha = M_\alpha\sum_{k=1}^{N_r}\nu_{\alpha k}\left(w_{kf} - w_{kb}\right) \tag{23}$$

The stoichiometric coefficient $\nu_{\alpha k} = \nu^f_{\alpha k} - \nu^b_{\alpha k}$ is expressed in terms of the forward stoichiometric coefficient $\nu^f_{\alpha k}$ and backward stoichiometric coefficient $\nu^b_{\alpha k}$. N_r represents the number of reactions. The forward and backward reaction rates are w_{kf} and w_{kb}, respectively. They are given by

$$w_{kf} = k_{fk}\prod_{\alpha=1}^{N_s}C_\alpha^{\nu^f_{\alpha k}}C_M^{\nu_M} \tag{24}$$

$$w_{kb} = k_{bk}\prod_{\alpha=1}^{N_s}C_\alpha^{\nu^b_{\alpha k}}C_M^{\nu_M} \tag{25}$$

where $C_\alpha = Y_\alpha\rho/M_\alpha$ is the concentration of species α, and C_M is the concentration of a collision partner (the exponent ν_M is one for third-body reactions and zero otherwise). Note that k_{fk} and k_{bk} are the rate constants of the forward and backward reactions, respectively; k_{bk} is computed by using k_{fk} and the chemical equilibrium constant. To close the filtered chemical source $\bar{S}_\alpha$ term in Eq. (12), two different model approaches are pursued in this work, which are based on Eq. (23). Firstly, an assumed probability density function (APDF) model proposed in [67,68] is used in one LES. In this statistical approach, the filtered chemical source term is modeled as an expectation on the basis of the APDF. This model requires the solution of two additional transport equations for subgrid-scale temperature variance and the trace of the subgrid-scale covariance matrix of species mass fraction. Secondly, a thickened flame model (TF) given in [69] is used. The thickness factor of the model is computed dynamically as suggested in [70], i.e., based on the ratio of the local grid size and the local thickness of a laminar premixed flame. The latter quantity is obtained here from computations of laminar, freely propagating premixed flames. The flame thickness data are tabulated as a function of mixture fraction for use in the TF model.

F. Boundary Conditions

An important aspect is the treatment of in- and outflow boundaries. Here we use the Navier–Stokes characteristic boundary conditions (NSCBC) approach [71]. In the present work, the fuel and air inflow boundaries are fully reflective since a constant mass flow rate is prescribed at these boundaries. Temperature and composition are taken to be constant at these inflow boundaries: the air temperature is 673.1 K, and the fuel temperature is 343.4 K. The composition of the fuel is given in Table 1; for air we assume an oxygen mass fraction of 0.23 and a nitrogen mass fraction of 0.77. The inflow and outflow of the exhaust plenum depicted in Fig. 1 are nonreflective.

Table 1 Composition of fuel

Species	Mass fraction
CH_4	0.626
H_2	0.220
C_2H_6	0.032
CO_2	0.096
N_2	0.026

The amplitudes of the incoming characteristic waves, i.e., L_2 to $L_{5+\alpha}$, are modeled at the nonreflective inflow boundaries as [62,64,71,72]

$$L_2 = -\sigma_2(\tilde{T} - \tilde{T}_{\text{trgt}}) \tag{26}$$

$$L_3 = \sigma_3(\tilde{u}_{t,1} - \tilde{u}_{t,1,\text{trgt}}) \tag{27}$$

$$L_4 = \sigma_4(\tilde{u}_{t,2} - \tilde{u}_{t,2,\text{trgt}}) \tag{28}$$

$$L_5 = \sigma_5(\tilde{u}_n - \tilde{u}_{n,\text{trgt}}) \tag{29}$$

$$L_{5+\alpha} = \sigma_{5+\alpha}(\tilde{Y}_\alpha - \tilde{Y}_{\alpha,\text{trgt}}) \tag{30}$$

In these equations, the vector $(u_n, u_{t,1}, u_{t,2})^T$ denotes the velocity vector at the boundary (the coordinates of this velocity vector are expressed for each boundary face in a local coordinate system that is aligned with the normal vector of a boundary face). The index trgt denotes target quantities that have to be specified. For the target temperature and target composition, we assume an adiabatic–isobaric chemical equilibrium (i.e., for an air–fuel mixture at an equivalence ratio of 0.625 and a pressure of 8 bar). The target normal velocity $u_{n,\text{trgt}}$ is set to 40 m/s, and the tangential velocity components $u_{t,1,\text{trgt}}$ and $u_{t,2,\text{trgt}}$ are set to 0 m/s. The model parameters σ_2 to $\sigma_{5+\alpha}$ are set to $\sigma_2 = 100\ \text{kg}/(\text{m}\cdot\text{s}^3\ \text{K})$, $\sigma_3 = \sigma_4 = 100\ \text{kg}/(\text{m}^2\cdot\text{s}^2)$, $\sigma_5 = 3\times10^5\ \text{kg}/(\text{m}^2\cdot\text{s}^2)$, and $\sigma_{5+\alpha} = 100\ \text{s}^{-1}$. For the outflow of the exhaust plenum, only one characteristic wave amplitude needs to be specified, i.e.,

$$L_1 = \sigma_1(1 - Ma^2)\frac{\bar{c}}{l}\left(\bar{p} - \bar{p}_{\text{trgt}}\right) \tag{31}$$

where the approach of [73] is used. The parameters for the outflow boundary (i.e., Mach number Ma, length scale l, target pressure $\bar{p}_{\text{trgt}}$, and model parameter σ_1) are $Ma = 0.17$, $l = 0.1075$ m, $\bar{p}_{\text{trgt}} = 8$ bar, and $\sigma_1 = 3$. All wall boundaries are acoustically fully reflective. They are assumed to be adiabatic with the exception of the combustion chamber walls. For the side walls forming the hexagon and the outflow duct, a constant temperature of 800 K is assumed. At the base plate of the combustion chamber, a constant temperature of 766.44 K is used (this value is obtained from measurements).

G. Reaction Mechanism

An important aspect in this LES is the reaction mechanism used to describe the oxidation of the hydrogen–natural gas mixture. The natural gas itself is a mixture of various gases (cf. Table 1). It appears to contain about 3% C_2H_6. Hence, a reaction mechanism is required that accurately describes the C2 chemistry as well as the chemistry of CH_4–H_2 mixtures. To this end, a reduced reaction mechanism is derived in this work from the DLR Concise reaction mechanism [74]. During the reduction process the reaction mechanism is validated against experimental data: Ignition delay times as well as laminar flame speeds of C_2H_6 and various mixtures of H_2 and CH_4 are considered at pressures ranging from 1 atm up to 60 atm. The resulting mechanism consists of 25 species and 126 reactions. Details on the reduction and results of its validation are available as supplementary material in Supp_Data_S1.pdf, and the reaction mechanism is available as supplementary materials in Supp_Data_S2.txt, Supp_Data_S3.txt, and Supp_Data_S4.txt.

IV. MRPOD Method

In this work the MRPOD method [51,52] is used to analyze the computational data. To compute the MRPOD, the LES solution is sampled during the limit cycle at a frequency of 20,000 Hz (the Nyquist frequency is 10,000 Hz). Each sample includes the solution variables in the entire computational domain. The spatial resolution of each sample is determined by the resolution of the computational grid. These samples are used to compute the correlation matrix for the MRPOD. To account for the nonuniformity of the computational grid, the correlation matrix for the MRPOD is weighted by the normalized size of the control volume as described in [75]. In the present work, the MRPOD is applied to the pressure and the velocity vector only. For the velocity vector, the correlation matrix is computed as described in [76]. Formally, the MRPOD of a variable $\zeta(x_i, t)$ in a frequency band I is expressed as

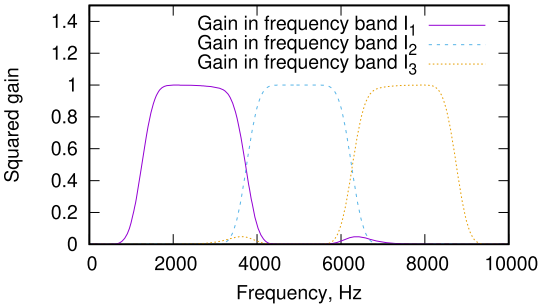

Fig. 5 Squared gain of filters in MODPWT.

$$\zeta(x_i, t)'_I = \sum_{k=1}^{N} a_{k,I}(\zeta, t)\phi_{k,I}(\zeta, x_i) \tag{32}$$

where N denotes the length of the time series, $a_{k,I}(\zeta, t)$ the kth temporal coefficient in the frequency band I, and $\phi_{k,I}(\zeta, x_i)$ the corresponding spatial mode. The operator $\bullet'$ denotes the fluctuation of a variable over its time average given by the operator $\langle\bullet\rangle$, i.e.,

$$\zeta(x_i, t) = \langle\zeta(x_i, t)\rangle + \zeta(x_i, t)' \tag{33}$$

To perform the MRA required for MRPOD, maximum-overlap discrete packet wavelet transform (MODPWT) is used, which is based here on Daubechies least asymmetric, compactly supported wavelet [77] with a filter length of 12, denoted by LA(12) [78]. For these wavelets, a decomposition level of three is employed; i.e., the frequency domain up to the Nyquist frequency of 10,000 Hz is divided into eight equally spaced scales (or frequency intervals) with a width of 1250 Hz. Since the gain of each individual wavelet filter does not provide a good approximation to a bandpass filter on all of these eight scales, we combine two filters on adjacent scales as outlined in [51]. In detail, the filters on the first and second, third and fourth, and fifth and sixth scales are combined with each other. The squared gain, which results from this combination of filters, is shown in Fig. 5. The wavelet filters act as bandpass filters on the nominal frequency bands $I_1 = [1717\ \text{Hz}; 3100\ \text{Hz}]$, $I_2 = [4218\ \text{Hz}; 5782\ \text{Hz}]$, and $I_3 = [6700\ \text{Hz}; 8400\ \text{Hz}]$, which are the relevant frequency ranges for HFI in this burner as discussed in Sec. V.

V. Results

A. Grid Study

In a first step, the grid dependency of the LES is investigated. For this purpose, LES with the TF model is performed on the coarse and the fine grid. The average values obtained from these computations, i.e., runs one and three in Table 2, are compared to assess the dependency of the solution on the grid resolution. This comparison is given in Fig. 6 for the average values of Favre-filtered temperature and Favre-filtered u_1 velocity. The data are plotted as a function of

Table 2 Overview on computational runs

Run	Closure for filtered chemical source term	Grid
1	Thickened flame	Coarse
2	Assumed probability density function	Coarse
3	Thickened flame	Fine

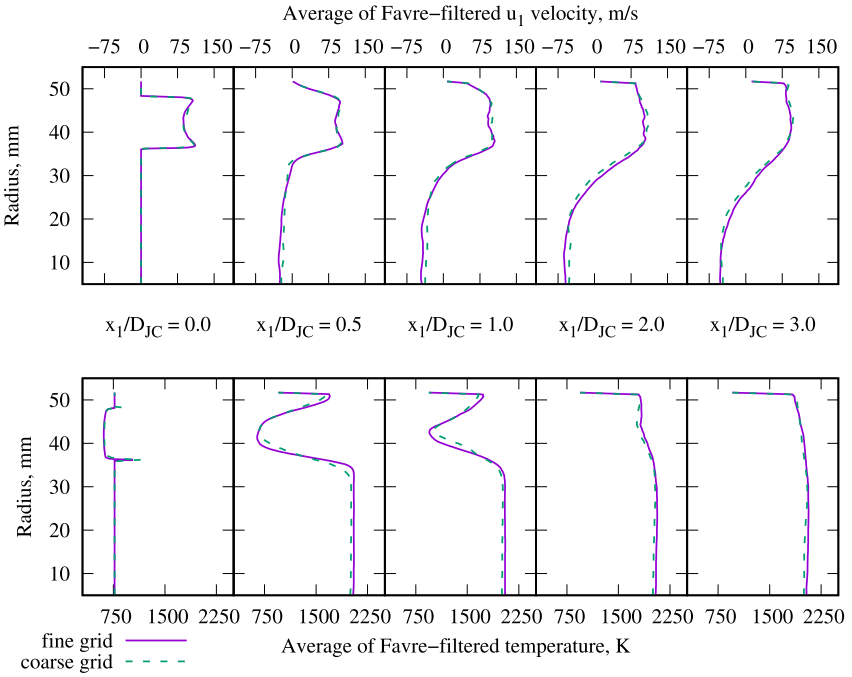

Fig. 6 Average value of Favre-filtered temperature and u_1 velocity for different grids (LES with TF model).

radius at five different locations x_1/D_{JC} downstream of the jet carrier exit plane. The coordinate system used to denote these locations is shown in Fig. 1, and the origin is located at the center of the combustion chamber's base plate. A jet carrier whose center is located at $x_2 \approx 11$ mm, and $x_3 \approx 41$ mm is considered in Fig. 6. The solutions on these two grids show only minimal differences and follow the same trend. A similar degree of agreement is found also at all other jet carriers in this burner. For this reason, the coarser grid is used in the subsequent investigations in order to reduce the computational cost of the simulations.

B. Frequency Spectrum

To assess the fidelity of the two different models for the filtered chemical source term (i.e., the APDF and the TF model), we investigate first the pressure in the combustion chamber. The relative pressure computed with these two models (i.e., runs one and two in Table 2) is shown in Fig. 7. The results are normalized with the operating pressure of 8 bar. Both computations are started from a reactive LES, which is performed with an incompressible pressure correction method (i.e., compressibility is neglected in this initial solution). In both computations the pressure oscillations grow initially exponentially over time, where a large growth rate is observed in the LES with the APDF model. In contrast to that, the pressure amplitudes computed with the TF model grow first slower over time but increase rapidly after approximately 0.02 s. The amplitude reaches maximal values between 0.03 and 0.04 s, where an "overshoot zone" is observed. This "overshoot zone" is followed by a limit cycle where pressure amplitude remains constant. Such an "overshoot zone" is missing in the LES with the APDF model. Instead, after approximately 0.035 s, the exponential amplitude growth of the pressure amplitude ceases, and the amplitude oscillations enter a limit cycle. Compared to the simulation with the TF model, the amplitude of the APDF model appears to be about 45% higher in the limit cycle. The measured normalized pressure is shown in Fig. 3 (curve "corrected signal"). A direct comparison of Figs. 7 and 3 shows that the measured amplitudes are about 2.2 times lower than the computed amplitudes of the TF model and even 3.2 times lower than the computed amplitudes of the APDF model. This overestimation of amplitudes by both computations is reflected in the amplitude spectral density (ASD) of pressure, which is shown in Fig. 8. In order to compute the ASD for each LES, a single data ensemble is used with a total of 140,000 data points. For a sampling frequency of 10 MHz, a spectral resolution of 71.4 Hz is obtained. A Hann window function is used to compute the ASD. The frequencies of the four major "peaks" observed in the experiment, i.e., 2390, 4770, 5670, and 7199 Hz, are captured extremely well by LES with both the APDF and TF models. Also, the amplitudes of the modes at 4770 and 7199 Hz are computed accurately by both models. The amplitude of the first mode at 2390 Hz is, however, clearly overestimated by both models. A noteworthy discrepancy between both LES and the experiment is the occurrence of a double peak in the experiment close to 2390 Hz. This peak is not reproduced by either LES. A closer analysis of the experimental data reveals that both modes are simultaneously present in the measured pressure; i.e., no switching between two

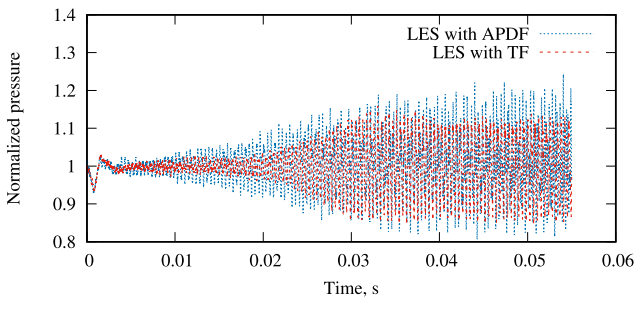

Fig. 7 Normalized computed pressure.

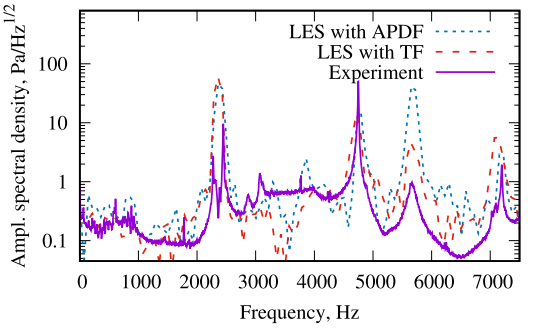

Fig. 8 Amplitude spectral density of pressure in the combustion chamber.

frequencies occurs. A possible explanation for why this double peak is not observed in LES is presented in Sec. V.D. At 5670 Hz, there appears to be a big difference between the results of the models. The amplitude of this mode is well reproduced by the LES with the TF model. The LES with the APDF model overestimates the amplitude by a large factor of almost 100. Since the LES with the TF model, i.e., run one in Table 2, appears to give the better agreement to available experimental data, we focus the following investigations on the results of this particular LES.

C. Averaged Fields of LES with TF Model

To provide an impression of the flowfield within the combustor, streamlines are shown in Fig. 9 for the LES with the TF model along with contour plots of averages of Favre-filtered OH mass fraction, temperature, heat release, and u_1 velocity. The computations have been run for 55 ms, which corresponds to about 7.8 residence times. The averaging is started once the limit cycle is reached, i.e., after 40.95 ms. The data shown in Fig. 9 are extracted in a plane at $x_2 = 11$ mm. It is clear from Fig. 9 that a recirculation zone is formed within the combustion chamber, which transports continuously hot combustion products back to the root of the flame and thus aids its stabilization. On average the flame appears to be anchored at the exit of the jet carrier, as the heat release indicates. This is in agreement with the experiment where, on average, compact anchored flames are observed at the exit of the jet carriers (cf. OH* chemiluminescence in Fig. 4).

D. Analysis of Pressure Modes for LES with TF Model

To elucidate the modes associated with the four frequencies presented in Sec. V.B, we perform an MRPOD of the computed pressure field as described in Sec. IV. Results for the spatial pressure modes $\phi_{k,I}(p)$ in each of the frequency bands I_1, I_2, and I_3 are given in Fig. 10. The first modes, i.e., $\phi_{1,I_1}(p)$, $\phi_{1,I_2}(p)$, and $\phi_{1,I_3}(p)$, contain most of the energy in these frequency bands, as an examination of the

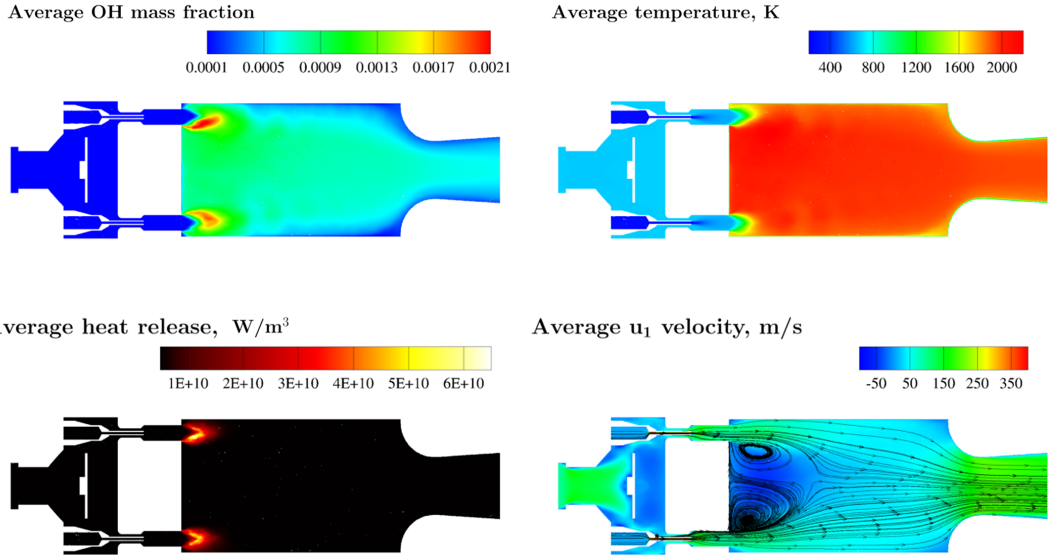

Fig. 9 Averaged fields of Favre-filtered OH mass fraction, temperature, heat release, and u_1 velocity (LES with TF model).

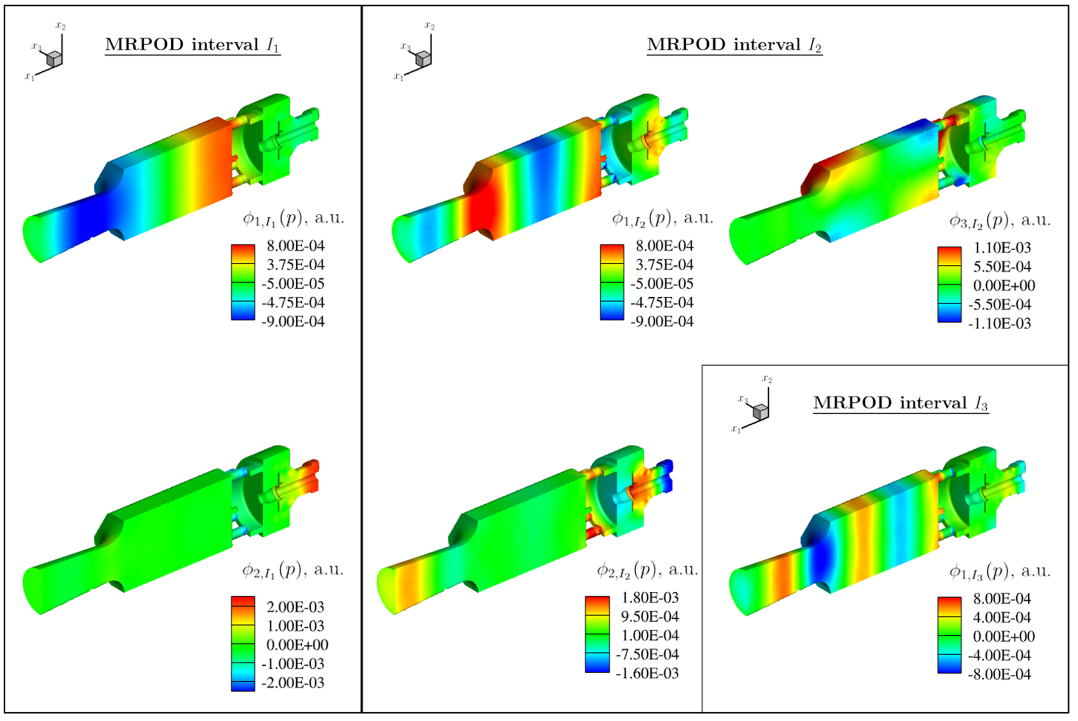

Fig. 10 MRPOD modes in burner. The data are extracted from LES with TF model.

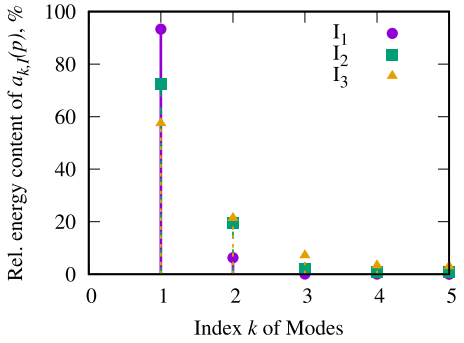

Fig. 11 Relative energy content.

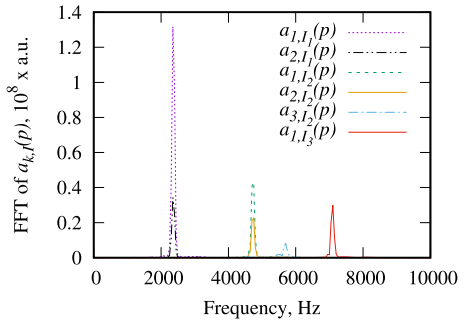

Fig. 12 FFT of the time coefficients.

relative energy content in Fig. 11 reveals. They contain between 57% and 94% of the energy. These three modes are purely longitudinal modes in the combustion chamber and outflow duct, where $\phi_{1,I_2}(p)$ and $\phi_{1,I_3}(p)$ are the second and third harmonics of $\phi_{1,I_1}(p)$. The frequencies of these three modes can be deduced from the fast Fourier transforms (FFT) of the temporal coefficients $a_{1,I_1}(p)$, $a_{1,I_2}(p)$, and $a_{1,I_3}(p)$, which is given in Fig. 12. It appears that the mode $\phi_{1,I_1}(p)$ oscillates at a frequency of 2390 Hz, whereas $\phi_{1,I_2}(p)$ and $\phi_{1,I_3}(p)$ oscillate at frequencies of 4770 and 7199 Hz, respectively. Hence, the HFI observed experimentally at these three frequencies is attributed to purely longitudinal modes. As shown in Fig. 12, the modes $\phi_{2,I_1}(p)$ and $\phi_{2,I_2}(p)$ contribute also to the HFI at 2390 and 4770 Hz. The mode $\phi_{2,I_1}(p)$ causes mainly HFI in the air plenum. It could be due to such a plenum mode that two peaks are observed experimentally at 2390 Hz, as shown in Fig. 8. In the MRPOD of the LES data, it is found that such a plenum mode may still cause low-amplitude pressure oscillations in the combustion chamber. The frequency of such a mode might depend on the modeling of the inflow boundary condition for the main air flow. In the LES presented here, we use a fully reflective inflow boundary condition as outlined in Sec. III.F. The use of a partially reflective inflow boundary might modify the frequency of this mode in such a way that two modes are ascertainable at 2390 Hz. Such a hypothesis requires, however, further verification. The mode $\phi_{2,I_2}(p)$ entails also a HFI in the plenum, which appears to be the second harmonic of $\phi_{2,I_1}(p)$ at a frequency of 4770 Hz. In addition, HFI are observed in the outflow duct as well as in the jet carriers. Both of these modes have a relatively low energy content compared to the first modes, as shown in Fig. 11 (approx. 6% for $\phi_{2,I_1}(p)$ and approx. 20% for $\phi_{2,I_2}(p)$). An exception to the aforementioned modes is the mode $\phi_{3,I_2}(p)$. This mode has a very low energy content compared to modes one and two in the frequency band I_2. Its energy content amounts to about 2%. This mode, however, is mainly responsible for the HFI observed at 5670 Hz, as the FFT of $a_{3,I_2}(p)$ in Fig. 12 shows. Compared to the other MRPOD modes, $\phi_{3,I_2}(p)$ is a mixed transverse–longitudinal mode. Its position appears to be stationary; i.e., no spinning in the transversal direction is found here (spinning requires a pair of modes at the same frequency, which is not found here). It is for this particular mixed transverse–longitudinal mode that the biggest differences between the LES with the APDF and TF model are found in Fig. 8. For the present burner configuration, it seems, therefore, that the computation of mixed HFI mode is particularly sensitive to the closure of the chemical source term in Eq. (12).

E. Investigation of Thermoacoustic Feedback Loop in LES with TF Model

In order to further the understanding of HFI in this burner, we investigate the thermoacoustic feedback loop between heat release and pressure oscillations based on the results of the LES with the TF model. For this purpose, the effects of fuel–air mixing and flowfield on heat release are examined in detail in the following subsections.

1. *Average Heat Release Distribution*

We consider first in Fig. 13 the average spatial distribution of heat release on a cylindrical surface of 42 mm radius, which intersects the jet carriers and the fuel nozzle. In contrast to Fig. 9 (where only two nozzles are shown in a planar contour plot), the left illustration in Fig. 13 clearly reveals that the spatial distribution of average heat release shows a rotational symmetry about the x_1 axis. For each flame anchoring at the exit of a jet carrier, the maximum heat release is found at point "C," as illustrated on the right of Fig. 13. Further, on the right, isolines of the average heat release are superimposed on a contour plot of the average u_1 velocity field. It appears that the average u_1 velocity field follows the same rotational symmetry about the x_1 axis. At the entrance of each jet carrier, two opposite sharp edges exist, as shown in Fig. 13, where flow separation bubbles denoted by "A" and "B" are formed. These flow separation bubbles have different sizes. The larger one is located at point "B," i.e., on the same side as point "C," where the maximum heat release is found. The larger size of the separation bubble at point "B" can be explained by the retarding effect of the large heat release at point "C." The large heat release at point "C" leads to a strong dilatation of the velocity field due to thermal expansion of the gases [79]. Due to this effect, the gas velocities ahead of point "C" are reduced. This

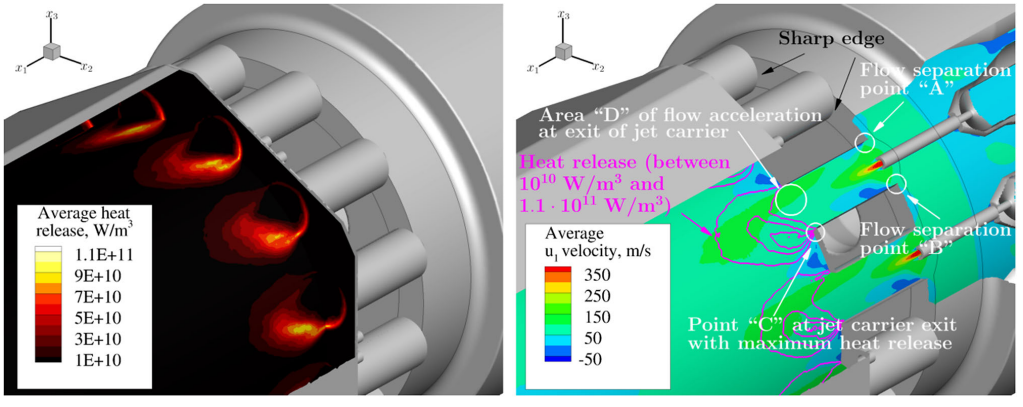

Fig. 13 Average heat release and u_1 velocity in combustion chamber.

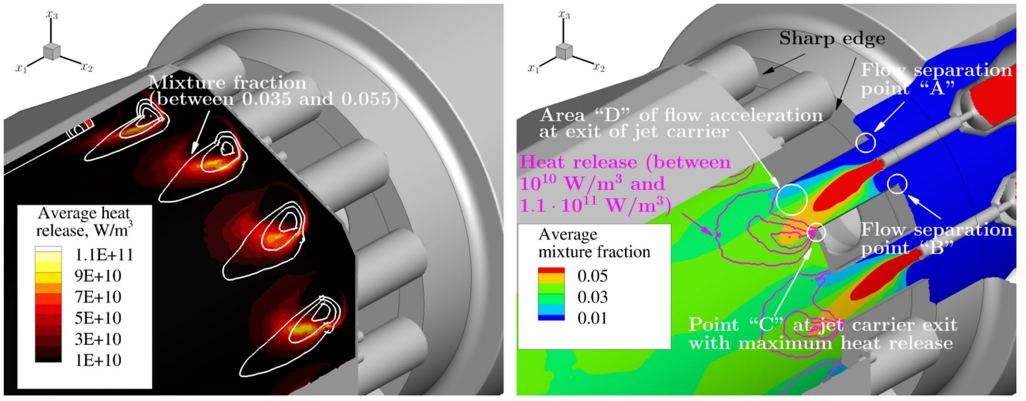

Fig. 14 Average heat release and mixture fraction in combustion chamber.

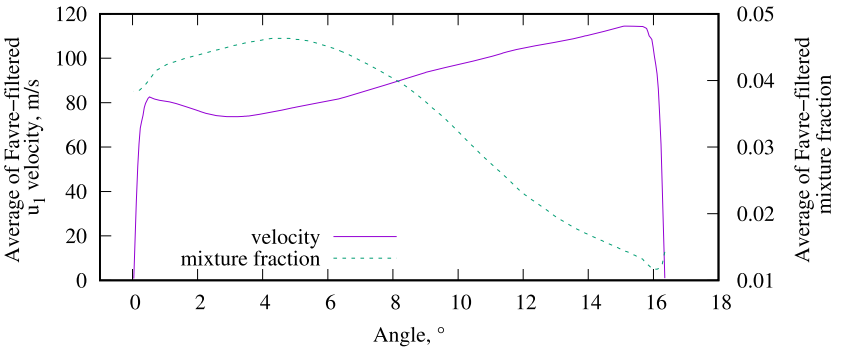

Fig. 15 Average value of Favre-filtered u_1 velocity and Favre-filtered mixture fraction at nozzle exit.

promotes the flow separation at point "B." Such a blockage of incoming flow by flow dilatation is also observed in [30]. A further consequence of this flow dilatation at point "C" is that the flow is being diverted toward the edge opposite of "C." This leads to an increased velocity in the area denoted by "D." This increase in flow velocity in the area "D" is accompanied by a reduction of heat release in this area (compared to the point "C"). Thus, the oncoming flow from edge "A" meets less flow resistance, and consequently the separation bubble is smaller compared to the one at point "B."

In a similar manner, the spatial distribution of average mixture fraction shows the same rotational symmetry about the x_1 axis (the mixture fraction definition given in [80] based on element mass fractions is used here). In Fig. 14, average mixture fraction is plotted along with average heat release on the same cylindrical surface as in Fig. 13. Fuel-rich areas, where the average mixture fraction is clearly above its global average value of 0.0302, coincide with the region of maximum heat release, as shown in the left illustration of Fig. 14. The mixing of fuel and air in the jet carriers is also affected by the hydrodynamic instabilities at the entrance of the jet carrier. As shown in the right illustration of Fig. 14, the transport of fuel is biased toward the side of the large separation bubble that is formed at the point "B." To quantify the effect of these flow separation bubbles on velocity and mixture fraction, average u_1 velocity and average mixture fraction are plotted in Fig. 15 along an arc of 42 mm radius spanning in the plane at $x_1 = 0$ m from "C" to "D." At an angle of 15.2° (this point is in the area "D"), average velocities of about 115 m/s are found, which exceed the velocity of 83 m/s at 0.5° (this point is in the area "C") by 39%. With regard to average mixture fraction, fuel-rich areas, where the global mixture fraction is exceeded by almost 50%, are found in Fig. 15 on average between 0° and 8°, i.e., in the region "C" of low average u_1 velocity. Beyond 11°, the average mixture fraction decreases below its global average value and reaches almost one-third of its global value at about 16°. This decrease coincides with the region "D" of high flow velocities. These results show that there is a direct relation between the flow separation bubbles at the inlet of a jet carrier and the average velocity and fuel distribution at its exit and, thus, on the spatial distribution of average heat release. The influence of these flow separations on the dynamic behavior of the heat release zone is investigated next.

2. *Dynamic Behavior of Heat Release Zone*

To show the time-resolved interaction between heat release and flowfield in more detail, both the instantaneous heat release and the instantaneous u_1 velocity obtained from LES are evaluated over the duration of a single pressure oscillation. Exemplary, one such pressure oscillation is extracted from the instantaneous LES results and shown in Fig. 16. In this figure, different points in time denoted by t_1 to t_6 are highlighted, which cover different phases of the pressure oscillation. Instantaneous images of heat release and u_1 velocity are shown in Fig. 17 for each of these points in time. At time t_1 the cycle begins in a pressure maximum, and we observe two separation bubbles at points "A" and "B." At this point in time, the largest heat release occurs in the proximity of point "C," resulting in a large separation bubble at point "B." As detailed in Sec. V.E.1, the dilatation caused by strong heat release at point "C" and the flow separation at point "B" sustain each other. In contrast, the opposite

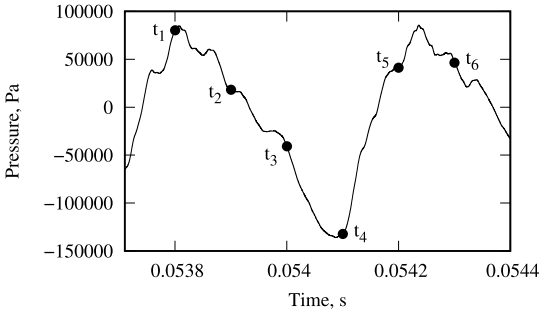

Fig. 16 Pressure in combustion chamber during one thermoacoustic cycle (obtained from LES with TF model).

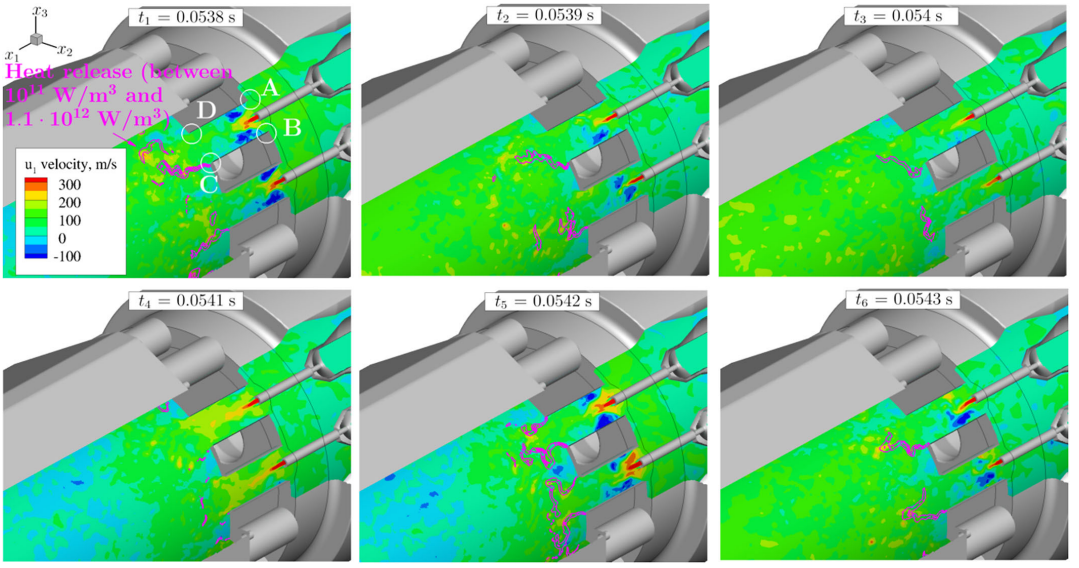

Fig. 17 Instantaneous heat release and u_1 velocity in combustion chamber during the pressure oscillation given in Fig. 16.

happens at points "A" and "D." Here, high flow velocities at point "D" coincide with flame blow-off, which leads (in the absence of strong flow dilatation at point "D") to a small separation bubble at point "A." This flow pattern prevails for the times t_2 and t_3. At time t_4, the pressure in the combustion chamber reaches its minimum (cf. Fig. 16), and the u_1 velocity in the jet carrier reaches its maximum value. At this point in time, the flame is almost completely blown off and the separation bubbles are diminished in size as the flow attaches to the walls. As the flow is forced to attach to the wall, the flow passing the sharp edges in "A" and "B" experiences strong centrifugal forces and begins again to separate. For this reason we observe again at the time point t_5 the formation of separation bubbles at both edges. Strong heat release appears now temporarily both in the points "C" and "D," and the pressure in the combustion chamber increases. At the time point t_6, the whole cycle starts from the beginning.

To show the dynamic processes involved in the mixing of fuel and air, the instantaneous mass fraction of fuel, i.e., the sum of the mass fractions of hydrogen, methane, and ethane, is shown in Fig. 18 together with isolines of instantaneous heat release over the entire cycle defined in Fig. 16. Compared to heat release, the periodic oscillation of fuel mass fraction cannot be easily ascertained from this image. However, Fig. 18 shows that at most of the points in time (except for t_5), fuel-lean conditions are found in the region "D," where the mass fraction is below its global value of 0.0265 (this global value corresponds to a fuel mass fraction where the streams of air and fuel are perfectly mixed). These lean conditions lead to a drop in flame speed, which, in combination with high flow speeds, favors flame blow-off in region "D." Significant heat release at "D" occurs only at the time t_5 when a reduction in flow velocity and an increase in fuel mass fraction happen to coincide in this area. By comparison, fuel-rich conditions with fuel mass fractions well above their global value prevail in the region "C." The resulting higher flame speed provides, in combination with low flow velocities, favorable conditions for flame stabilization. It is for this reason that we observe in Figs. 17 and 18 almost for all points in time a flame that is preferentially anchored at "C" and that is distorted by the turbulent flow conditions. The only exception is time t_4, where, despite the presence of sufficient fuel, the flame is blown off by the flow.

These observations made on the basis of a single cycle can also be substantiated statistically on the basis of phase averages for minimum and maximum pressure points in time, such as t_1 and t_4. Contour plots of phase-averaged fuel mass fraction and u_1 velocity are summarized in Fig. 19. The phase averages for minimum pressure confirm that a low amount of fuel at point "C" coincides,

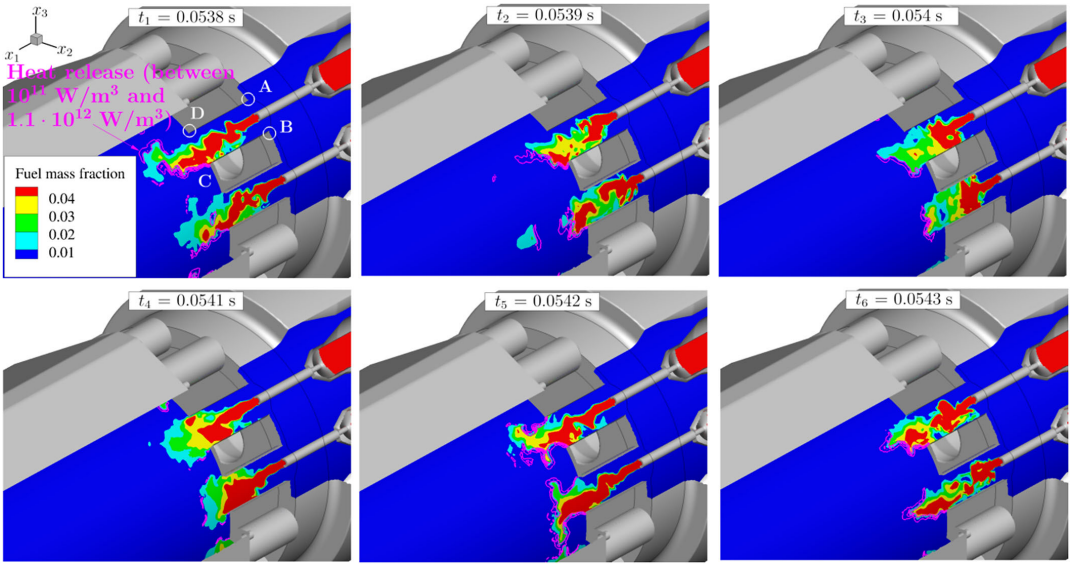

Fig. 18 Instantaneous heat release and fuel mass fraction in combustion chamber during the pressure oscillation given in Fig. 16.

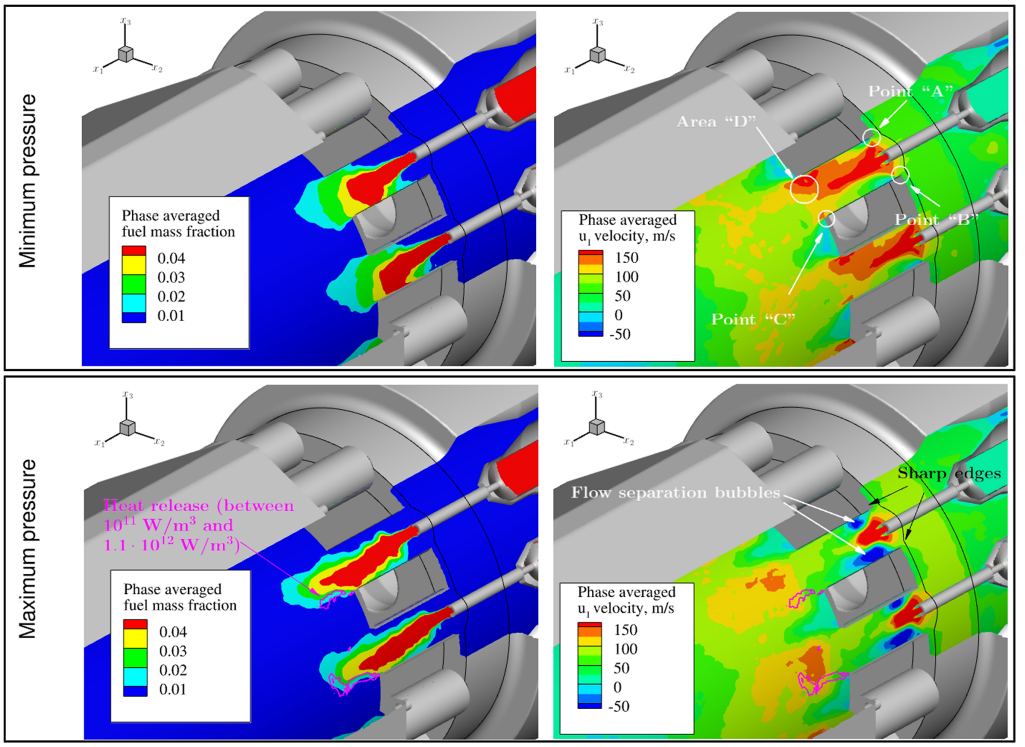

Fig. 19 Phase averages of fuel mass fraction, u_1 velocity, and heat release for phases of minimum and maximum pressure.

on average, with high u_1 velocities at point "C" and in the area "D." Isolines of phase-averaged heat release are not visible at minimum pressure since the maximum of average heat release is below the threshold value of 10^{11} W/m^3 for the isolines. For phases of maximum pressure, the situation is reversed; i.e., the flow velocity at point "C" and in region "D" is low, and the fuel mass fraction at point "C" is high. In agreement with the behavior observed for a single cycle, the heat release is highest at point "C" during phases of maximum pressure, where on average a flame sheet appears to be anchored. During phases of maximum pressure, the phase average of u_1 velocity confirms the presence of a small flow separation bubble downstream of point "A" and a larger one downstream of point "B." These flow separations almost disappear during phases of minimum pressure. Profiles of phase-averaged u_1 velocity and fuel mass fraction are plotted in Fig. 20 along an arc of 42 mm radius spanning in the plane at $x_1 = 0$ m from "C" to "D." The drastic rise in u_1 velocity from phases of maximum pressure to phases of minimum pressure is clearly recognizable with increases of at least 30% and up to 66%. Likewise, very fuel-rich conditions are found during phases of maximum pressure with fuel mass fractions of almost double the global value. By comparison, during phases of minimum pressure, the fuel mass fraction is close to the global value, deviating by at most 20%.

To summarize the findings, the flow separation bubbles at the entrance of the jet carrier are critical for the flame stabilization in the burner. They cause at the exit of each jet carrier an inhomogeneous distribution of flow velocity and lead to poor mixing of air and fuel. This is manifested in the asymmetrical profiles of average u_1 velocity and average mixture fraction at the exit plane of the jet carrier (cf. Fig. 15). As a direct consequence, the flame is only able to anchor in the regions of low flow velocity and high fuel content. In regions with less fuel, it appears to be susceptible to blow off. This explains the rotational symmetry of average heat release observed in Figs. 13 and 14.

To shed more light on the dynamics of these hydrodynamic instabilities, we investigate the u_1 velocity field with the help of MRPOD. Results for different modes in the frequency bands I_1 and I_2 are summarized in Fig. 21; the FFT of the temporal coefficients and the relative energy content for each mode are summarized in Figs. 22 and 23. Due to the strong pressure oscillations, most of the energy is concentrated in the first modes $\phi_{1,I_1}(u_1)$ and $\phi_{1,I_2}(u_1)$. The hydrodynamic instabilities in the region of the jet carrier are

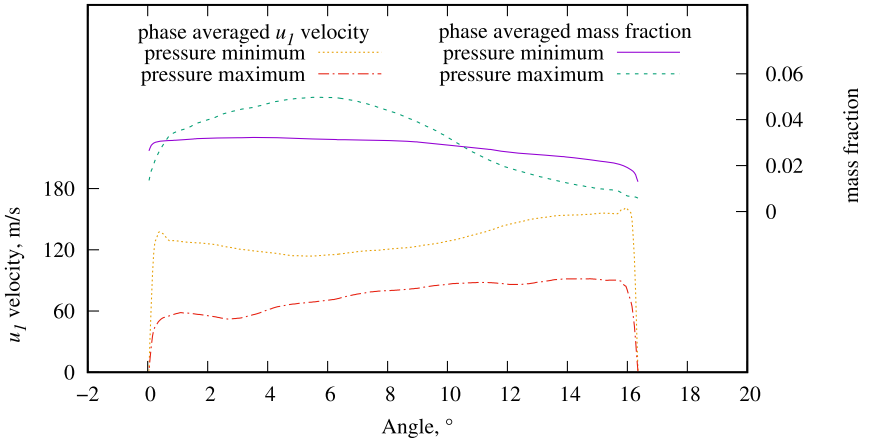

Fig. 20 Phase-averaged value of Favre-filtered u_1 velocity and Favre-filtered fuel mass fraction at nozzle exit.

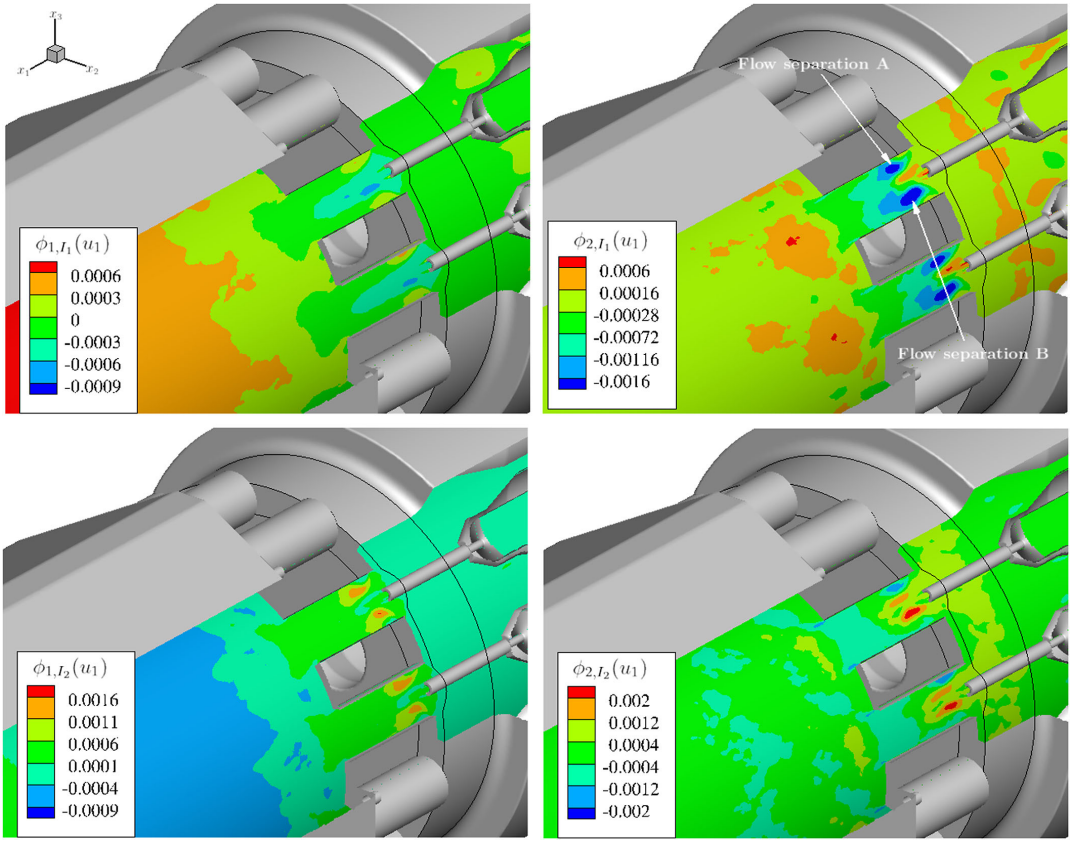

Fig. 21 MRPOD modes of u_1 velocity in combustion chamber.

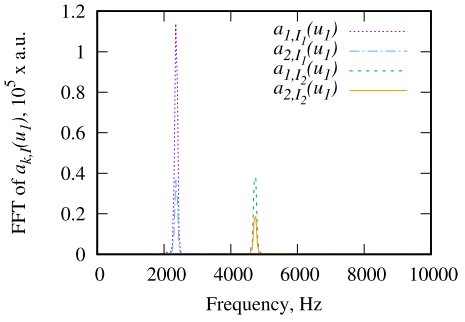

Fig. 22 FFT of the time coefficients.

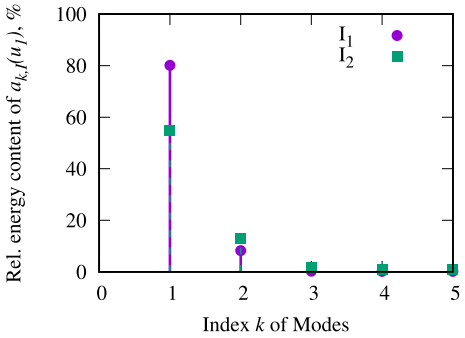

Fig. 23 Relative energy content.

contained in the second MRPOD modes $\phi_{2,I_1}(u_1)$ and $\phi_{2,I_2}(u_1)$. From the contour plot in Fig. 21, it is clear that the dynamics of the separation bubble are mainly contained in $\phi_{2,I_1}(u_1)$. In this illustration the different sizes of the separation bubbles "A" and "B" can be clearly ascertained. The frequency f of the separation is found to equal 2390 Hz, i.e., the frequency of the first longitudinal mode. This corresponds to a diameter-based jet carrier Strouhal number of $St_{\mathrm{JC}} = fD_{\mathrm{JC}}/U_{\mathrm{JC}} \approx 0.24$ (for a jet carrier velocity scale $U_{\mathrm{JC}} = 120$ m/s). This dimensionless frequency equals typical values found in other flows with hydrodynamic instabilities (e.g., flows in a bent pipe [81,82] and axisymmetric jet flows [83]).

3. *Heat Release Fluctuations*

In a final step we examine the heat release fluctuations. To identify different causes for heat release fluctuations, we follow the approach in [84] and distinguish between effects that modify the local internal structure of the reaction zone and its global geometry. Concerning the latter effect, the modification of geometry, it is already clear from Figs. 17 and 18 that, due to blow-off and distortions of the flame, the reaction zone geometry undergoes drastic changes during a single pressure oscillation. To quantify the overall distortion of geometry, we compute the overall volume of the reaction zone $V_{RZ}(t)$ in this burner as a function of time. For this purpose, we define an indicator function $\mathfrak{I}$ of the heat release zone as

$$\mathfrak{I}(x_i, t) = \begin{cases} 1, & \text{if } \mathfrak{S}(x_i, t) > \varepsilon_{\mathfrak{S}} \\ 0, & \text{else} \end{cases} \tag{34}$$

where $\mathfrak{S}$ is a sensor function of heat release and $\varepsilon_{\mathfrak{S}} = 10^{-4}$ a lower threshold value for this sensor. The sensor $\mathfrak{S}$ for the heat release zone is given by

$$\mathfrak{S}(x_i, t) = \max\left(\frac{4}{3}\tanh\left(\frac{\bar{\mathfrak{q}}(x_i, t)}{\mathfrak{q}_0}\right) - \frac{1}{3}, 0\right) \tag{35}$$

in terms of the local filtered heat release $\overline{\mathfrak{q}}$ and its reference value $\mathfrak{q}_0 = 30$ W/mm^3. This function is positive within the reaction zone and zero elsewhere. To check the accuracy of this sensor definition, we verify that the region identified by this sensor contains most of the global heat release. The volume of the reaction zone $V_{RZ}(t)$ is obtained by integration of the indicator function in Eq. (34) over the volume of the entire computational domain V_{CD}, i.e.,

$$V_{RZ}(t) = \int_{V_{CD}} \Im(x_i, t)\, \mathrm{d}V \tag{36}$$

where V is the volume in this equation. $V_{RZ}(t)$ is plotted together with the global heat release $Q(t)$, which is defined as

$$Q(t) = \int_{V_{CD}} \dot{\mathfrak{q}}(x_i, t)\, \mathrm{d}V \tag{37}$$

in Fig. 24. Both the reaction zone volume and heat release are in phase. During the limit cycle, the reaction zone volume falls below its mean value by approx. 40% and exceeds it by up to 60%, which represents a significant disturbance. The velocity fluctuations, which contribute to these fluctuations in reaction zone volume via flame blow-off, are related partly to the acoustic velocity at the exit of the jet carrier. To demonstrate this, we define first at the exit plane $x_1 = 0$ m of the jet carriers the area averages of Favre-filtered u_1 velocity and filtered pressure, i.e., $\{u_1\}_A(t)$ and $\{p\}_A(t)$, as

$$\{u_1\}_A(t) = \frac{1}{A_{\mathrm{JC}}} \int_{A_{\mathrm{JC}}} \tilde{u}_1(x_i, t)\, \mathrm{d}A \tag{38}$$

$$\{p\}_A(t) = \frac{1}{A_{\mathrm{JC}}} \int_{A_{\mathrm{JC}}} \bar{p}(x_i, t)\, \mathrm{d}A \tag{39}$$

and compute their temporal fluctuations $\{u_1\}'_A(t)$ and $\{p\}'_A(t)$. The area integration in Eqs. (38) and (39) is performed across the cross-sectional area of the jet carriers A_{JC}. Based on $\{p\}'_A(t)$, the acoustic velocity $u_{ac}(t)$ induced by the pressure wave is defined as $u_{ac}(t) \approx -\{p\}'_A(t)/(\rho_0 c_0)$. This definition assumes that the acoustic velocity is caused by a disturbance traveling upstream of the combustion chamber into the jet carrier (i.e., in negative x_1 direction). The reference density ρ_0 and reference speed sound c_0 are computed for a perfectly mixed state of fuel and air, yielding $\rho_0 = 4$ kg/m^3 and $c_0 = 512$ m/s. Figure 25 plots u_{ac} and $\{u_1\}'_A(t)$ alongside the global heat release $Q(t)$ and combustion chamber pressure $p_{CC}(t)$. Both $Q(t)$ and $p_{CC}(t)$ are in phase in the limit cycle. As discussed in Sec. V.E.2, global heat release reaches its minimum value when the u_1 velocity reaches its maximum value and blow-off occurs. At these time instances, the fluctuation $\{u_1\}'_A(t)$ and the acoustic velocity $u_{ac}(t)$ are both in phase and follow the same temporal evolution, reaching the same peak values between 50 and 70 m/s, as depicted in Fig. 25. This indicates a velocity coupling between heat release fluctuations and pressure oscillations, i.e., the increase of velocity, which ultimately contributes to flame blow-off, is caused directly by acoustic velocity.

Another important factor adding to heat release fluctuations are changes in the internal structure of the flame. To quantify this at least to some extent, we investigate the fluctuation of mixture

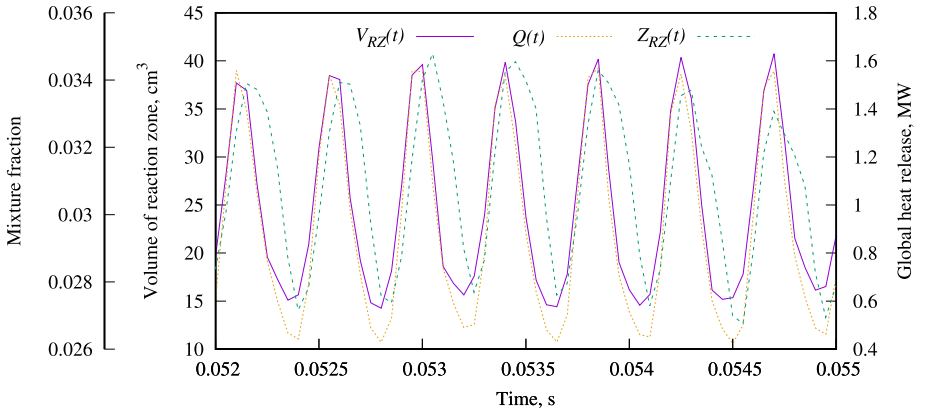

Fig. 24 Plot of global heat release $Q(t)$, volume of reaction zone $V_{RZ}(t)$, and mixture fraction in reaction zone $Z_{RZ}(t)$.

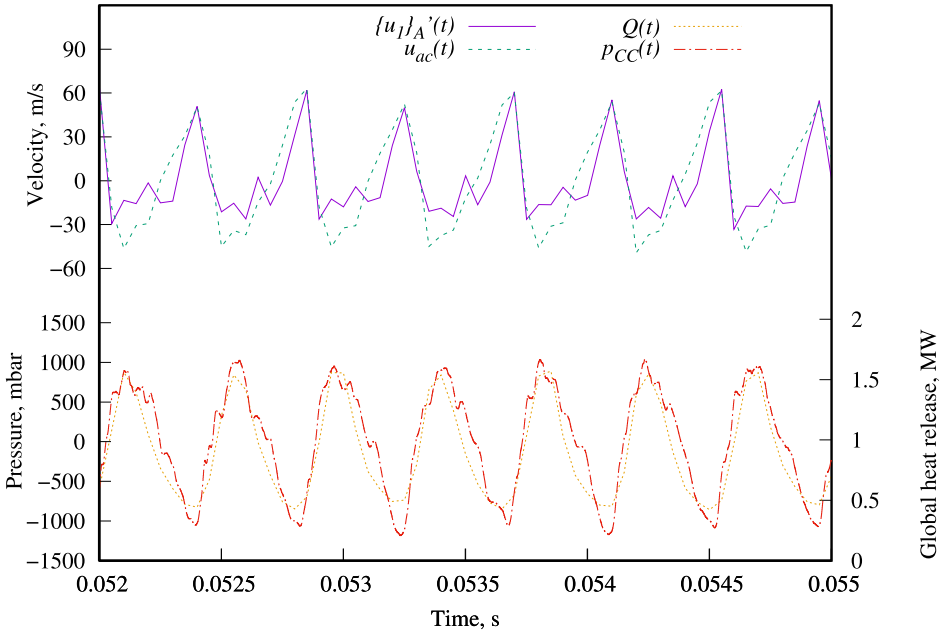

Fig. 25 Plot of velocity fluctuations (acoustic and area average) at exit of jet carrier, global heat release, and combustion chamber pressure.

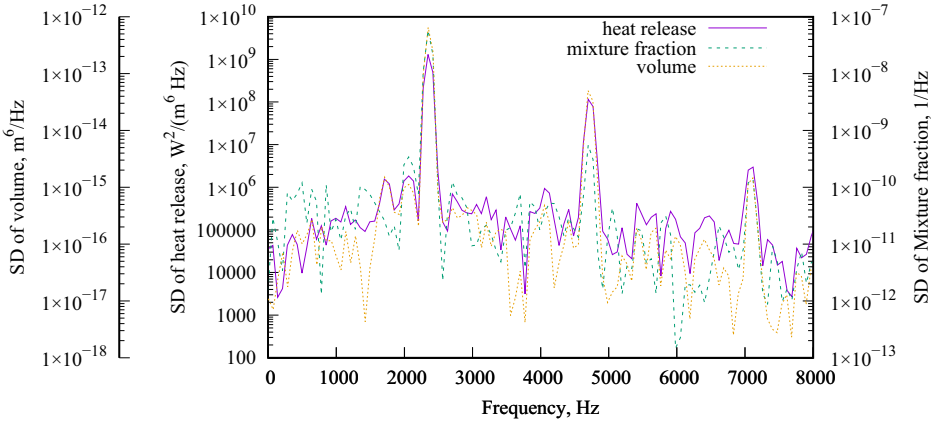

Fig. 26 Spectral densities of global heat release $Q(t)$, mixture fraction in reaction zone $Z_{RZ}(t)$, and volume of reaction zone $V_{RZ}(t)$.

fraction (i.e., equivalence ratio) in the reaction zone. To this end, we compute the mixture fraction in the reaction zone $Z_{RZ}(t)$ as

$$Z_{RZ}(t) = \frac{\int_{V_{CD}} \Im(x_i,t)\bar{\rho}(x_i,t)\tilde{Z}(x_i,t)\,\mathrm{d}V}{\int_{V_{CD}} \Im(x_i,t)\bar{\rho}(x_i,t)\,\mathrm{d}V} \tag{40}$$

where $\tilde{Z}$ is the Favre-filtered mixture fraction. Figure 24 plots this mixture fraction versus time. An FFT analysis shows that the mixture fraction appears to be lagging behind global heat release by a phase angle of 49°, which corresponds to a time lag of about 60 μs. The mixture fraction oscillations amount to about 10% of the mean value, which is less in comparison to the fluctuations in the volume of the reaction zone. However, to relate quantitatively this mixture fraction fluctuation to heat release fluctuations, we retrieve for the mean, minimum, and maximum value of mixture fraction the heat release from calculations of laminar premixed flames at these three mixture fractions. In order to account for the effect of strain rate on heat release, we compute steady one-dimensional premixed counterflow flames using the software Cantera [85]. The computations are performed for 8 bar pressure, and the temperature and composition of fuel and air for the stream of reactants are set to the same values as in the LES. The thermodynamic state of the opposing flow is obtained from the chemical equilibrium of the premixed reactants. By considering steady laminar flames, we neglect, based on [86], the influence of pressure fluctuations on heat release for the present conditions. From these computations a heat release of 68 W/mm^3 (which is an average value across the reaction zone) is obtained for the mean mixture fraction of 0.0302. For mixture fractions of 0.0272 (i.e., 10% below the mean value) and 0.0332 (i.e., 10% above the mean value), heat releases of 56 and 84 W/mm^3 are found, respectively. Thus, a deviation of 10% from the mean mixture fraction can decrease the heat release by about 18% and increase it by 24%, which is not negligible. Fluctuations in the local equivalence ratio add, therefore, considerably to the overall fluctuation of heat release in this LES. With regard to the oscillation frequency of $Q(t)$, $Z_{RZ}(t)$, and $V_{RZ}(t)$, the spectral densities (SD) are shown in Fig. 26. For all these variables, the highest energy of the oscillations is contained at 2390 Hz, i.e., the frequency of the first longitudinal mode of the pressure oscillations. The second and third harmonics of the frequency 2390 Hz, i.e., 4770 and 7199 Hz, contribute, at lower levels, also energy to the oscillations. Thus, the distribution of energy on different modes is, for these variables, similar to the energy distribution of pressure oscillations given in Fig. 8.

VI. Conclusions

In the present work, compressible LES of reactive flow is used to investigate HFI in a 12-nozzle jet-stabilized gas turbine burner that is operated at 8 bar at globally lean conditions with a mixture of hydrogen and natural gas. The set of governing equations is solved numerically using the ICS-WAF scheme. In- and outflow boundary conditions are handled via the NSCBC approach. LES results obtained with two different models for the filtered chemical source term, namely an APDF and a TF model, are compared to experimental data for pressure, which are obtained in this work for the first time in this particular burner. It is found in the experiments that HFI occurs at four frequencies of 2390, 4770, 5670, and 7199 Hz. These frequencies are reproduced accurately by the compressible LES with both the APDF and TF models. The measured amplitudes of the HFI appear to be well reproduced by the use of the TF model with the exception of the amplitude of the first mode at 2390 Hz, which is overestimated. The APDF model strongly overestimates the amplitude of the third mode at 5670 Hz as well as the amplitude of the first mode at 2390 Hz.

Since the LES with the TF model appears to give a good agreement to available experimental data, the results of this LES are analyzed further in order to understand the modes of HFI and the thermoacoustic feedback cycle. Using MRPOD, it is found that the frequencies of 2390, 4770, and 7199 Hz are associated with a longitudinal mode in the combustion chamber and its higher harmonics, whereas the frequency of 5670 Hz corresponds to the first mixed transverse–longitudinal mode in the combustion chamber. It is for this mixed mode that the APDF and TF model show the largest differences in pressure amplitude. It is therefore concluded that for the present burner, the choice of model for the filtered chemical source term is crucial for capturing correctly the amplitudes of transverse HFI modes. Analysis of the thermoacoustic feedback based on the data of the TF model reveals that the HFI is mainly caused by periodic distortions of flame geometry and fluctuations in equivalence ratio. Both occur at 2390, 4770, and 7199 Hz and contribute to the fluctuation of global heat release. Acoustic velocity plays an important role in distorting the flame since it leads to flame blow-off when combustion chamber pressure is at its minimum. Flow separation bubbles, i.e., hydrodynamic instabilities that occur periodically at 2390 Hz at the entrance of each jet carrier, also indirectly play a role in the feedback loop. They cause an inhomogeneous velocity and fuel distribution in the jet carriers, favoring, thus, the periodic blow-off of the flame. These inhomogeneities manifest themselves in a rotational symmetry of average heat release about the burner axis.

These LES results indicate different measures to prevent the occurrence of HFI in this burner. The suppression of the hydrodynamic instabilities by modifying the entrance to the jet carriers could be a first step in order to reduce the unmixedness in the stream of reactants and in order to dampen fluctuations in equivalence ratio. With regard to improving the mixing, it could also be useful to increase the length of the jet carriers. A better mixing of fuel and air might, in addition, prove useful for flame stabilization and, thus, for reducing the distortion of flame geometry.

Acknowledgments

The authors gratefully acknowledge the scientific support and HPC resources provided by the German Aerospace Center (DLR). The HPC system Computer for Advanced Research in Aerospace is partially funded by the Ministry of Science and Culture of Lower Saxony and the Federal Ministry for Economic Affairs and Climate Action.

References

[1] Zinn, B. T., and Lieuwen, T. C., "Combustion Instabilities: Basic Concepts," *Combustion Instabilities in Gas Turbine Engines: Operational Experience, Fundamental Mechanisms, and Modeling*, Vol. 210, Progress in Astronautics and Aeronautics, AIAA, Reston, VA, 2005, pp. 1–26, Chap. 1.
https://doi.org/10.2514/4.866807

[2] Huang, Y., and Yang, V., "Dynamics and Stability of Lean-Premixed Swirl-Stabilized Combustion," *Progress in Energy and Combustion Science*, Vol. 35, No. 4, 2009, pp. 293–364.
https://doi.org/10.1016/j.pecs.2009.01.002

[3] Goy, C. J., James, S. R., and Rea, S., "Monitoring Combustion Instabilities: E.ON UK's Experience," *Combustion Instabilities in Gas Turbine Engines: Operational Experience, Fundamental Mechanisms, and Modeling*, Vol. 210, AIAA, Reston, VA, 2005, pp. 163–175, Chap. 8.
https://doi.org/10.2514/4.866807

[4] Sewell, J. B., and Sobieski, P. A., "Monitoring of Combustion Instabilities: Calpine's Experience," *Combustion Instabilities in Gas Turbine Engines: Operational Experience, Fundamental Mechanisms, and Modeling*, Vol. 210, Progress in Astronautics and Aeronautics, AIAA, Reston, VA, 2005, pp. 147–162, Chap. 7.
https://doi.org/10.2514/4.866807

[5] Kaskan, W. E., and Noreen, A. E., "High-Frequency Oscillations of a Flame Held by a Bluff Body," *Transactions of the American Society of Mechanical Engineers*, Vol. 77, No. 6, 1955, pp. 885–891.
https://doi.org/10.1115/1.4014536

[6] Rogers, D., and Marble, F., "A Mechanism for High-Frequency Oscillation in Ramjet Combustors and Afterburners," *Journal of Jet Propulsion*, Vol. 26, No. 6, 1956, pp. 456–462.
https://doi.org/10.2514/8.7049

[7] Oefelein, J. C., and Yang, V., "Comprehensive Review of Liquid-Propellant Combustion Instabilities in F-1 Engines," *Journal of Propulsion and Power*, Vol. 9, No. 5, 1993, pp. 657–677.
https://doi.org/10.2514/3.23674

[8] Culick, F. E., and Yang, V., "Overview of Combustion Instabilities in Liquid-Propellant Rocket Engines," *Liquid Rocket Engine Combustion Instability*, Vol. 169, Progress in Astronautics and Aeronautics, AIAA, Reston, VA, 1995, pp. 3–37, Chap. 1.
https://doi.org/10.2514/5.9781600866371.0003.0037

[9] Poinsot, T., "Prediction and Control of Combustion Instabilities in Real Engines," *Proceedings of the Combustion Institute*, Vol. 36, No. 1, 2017, pp. 1–28.
https://doi.org/10.1016/j.proci.2016.05.007

[10] Matsuyama, S., Shinjo, J., Ogawa, S., and Mizobuchi, Y., "Large Eddy Simulation of High-Frequency Combustion Instability of Supercritical LO_x/GH_2 Flame," *Proceedings of the 46th AIAA/ASME/SAE/ASEE Joint Propulsion Conference*, AIAA Paper 2010-6567, 2010.
https://doi.org/10.2514/6.2010-6567

[11] Feldman, T., Harvazinski, M., Merkle, C., and Anderson, W., "Comparison Between Simulation and Measurement of Self-Excited Combustion Instability," *Proceedings of the 48th AIAA/ASME/SAE/ASEE Joint Propulsion Conference & Exhibit*, AIAA Paper 2012-4088, 2012.
https://doi.org/10.2514/6.2012-4088

[12] Harvazinski, M., Xia, G., Anderson, W., and Merkle, C., "Analysis of Self-Excited Combustion Instability Using a Combination of Two- and Three-Dimensional Simulations," *Proceedings of the 50th AIAA Aerospace Sciences Meeting Including the New Horizons Forum and Aerospace Exposition*, AIAA Paper 2012-0782, 2012.
https://doi.org/10.2514/6.2012-782

[13] Matsuyama, S., Shinjo, J., Ogawa, S., and Mizobuchi, Y., "LES of High-Frequency Combustion Instability in a Single Element Rocket Combustor," *Proceedings of the 50th AIAA Aerospace Sciences Meeting Including the New Horizons Forum and Aerospace Exposition*, AIAA Paper 2012-1271, 2012.
https://doi.org/10.2514/6.2012-1271

[14] Garby, R., Selle, L., and Poinsot, T., "Large-Eddy Simulation of Combustion Instabilities in a Variable-Length Combustor," *Comptes Rendus Mecanique*, Vol. 341, Nos. 1–2, 2013, pp. 220–229.
https://doi.org/10.1016/j.crme.2012.10.020

[15] Matsuyama, S., Shinjo, J., and Mizobuchi, Y., "LES of High-Frequency Combustion Instability in a Rocket Combustor," *Proceedings of the 51st AIAA Aerospace Sciences Meeting Including the New Horizons Forum and Aerospace Exposition*, AIAA Paper 2013-0564, 2013.
https://doi.org/10.2514/6.2013-564

[16] Harvazinski, M. E., Talley, D. G., and Sankaran, V., "Comparison of a Structured-LES and an Unstructured-DES Code for Predicting Combustion Instabilities in a Longitudinal Mode Rocket Combustor," *Proceedings of the 53rd AIAA Aerospace Sciences Meeting*, AIAA Paper 2015-1608, 2015.
https://doi.org/10.2514/6.2015-1608

[17] Harvazinski, M. E., Huang, C., Sankaran, V., Feldman, T. W., Anderson, W. E., Merkle, C. L., and Talley, D. G., "Coupling Between Hydrodynamics, Acoustics, and Heat Release in a Self-Excited Unstable Combustor," *Physics of Fluids*, Vol. 27, No. 4, 2015, Paper 045102.
https://doi.org/10.1063/1.4916673

[18] Sardeshmukh, S. V., Heister, S. D., and Anderson, W. E., "Prediction of Combustion Instability with Detailed Chemical Kinetics," *Proceedings of the 53rd AIAA Aerospace Sciences Meeting*, AIAA Paper 2015-1826, 2015.
https://doi.org/10.2514/6.2015-1826

[19] Urbano, A., Selle, L., Staffelbach, G., Cuenot, B., Schmitt, T., Ducruix, S., and Candel, S., "Exploration of Combustion Instability Triggering Using Large Eddy Simulation of a Multiple Injector Liquid Rocket Engine," *Combustion and Flame*, Vol. 169, 2016, pp. 129–140.
https://doi.org/10.1016/j.combustflame.2016.03.020

[20] Nguyen, T. M., Popov, P. P., and Sirignano, W. A., "Driving Mechanisms of Liquid-Propellant Rocket Longitudinal Combustion Instability," *Proceedings of the 55th AIAA Aerospace Sciences Meeting*, AIAA Paper 2017-0822, 2017.
https://doi.org/10.2514/6.2017-0822

[21] Schmitt, T., Staffelbach, G., Ducruix, S., Gröning, S., Hardi, J., and Oschwald, M., "Large-Eddy Simulations of a Sub-Scale Liquid Rocket Combustor: Influence of Fuel Injection Temperature on Thermo-Acoustic Stability," *Proceedings of the 7th European Conference for Aeronautics and Aerospace Sciences (EUCASS)*, 2017.
https://doi.org/10.13009/EUCASS2017-352

[22] Urbano, A., Douasbin, Q., Selle, L., Staffelbach, G., Cuenot, B., Schmitt, T., Ducruix, S., and Candel, S., "Study of Flame Response to Transverse Acoustic Modes from the LES of a 42-Injector Rocket Engine," *Proceedings of the Combustion Institute*, Vol. 36, No. 2, 2017, pp. 2633–2639.
https://doi.org/10.1016/j.proci.2016.06.042

[23] Sardeshmukh, S. V., Bedard, M. J., Lorente, A. P., and Anderson, W. E., "Investigating Heat Release Dynamics in a Self-Excited Unstable Combustor Using High Fidelity Chemiluminescence Measurements and Modeling," *Proceedings of the 2018 AIAA Aerospace Sciences Meeting*, AIAA Paper 2018-1184, 2018.
https://doi.org/10.2514/6.2018-1184

[24] Lechtenberg, A., and Gerlinger, P. M., "Numerical Investigation of Combustion Instabilities in a Rocket Combustion Chamber with Supercritical Injection Using a Hybrid RANS/LES Method," *Proceedings of the AIAA Scitech 2020 Forum*, AIAA Paper 2020-1162, 2020.
https://doi.org/10.2514/6.2020-1162

[25] Hwang, W. S., Sung, B. K., Han, W., Huh, K. Y., Lee, B. J., Han, H. S., Sohn, C. H., and Choi, J. Y., "Real-Gas-Flamelet-Model-Based Numerical Simulation and Combustion Instability Analysis of a GH2/LOX Rocket Combustor with Multiple Injectors," *Energies*, Vol. 14, No. 2, 2021, p. 419.
https://doi.org/10.3390/en14020419

[26] Hasti, V. R., and Ranjan, R., "Computational Study of Longitudinal Combustion Instability in a High-Pressure Combustor," *Proceedings of the AIAA SCITECH*, AIAA Paper 2022-2087, 2022.
https://doi.org/10.2514/6.2022-2087

[27] Sharma, A., De, A., and Kumar, S. S., "Numerical Investigation of Supercritical Combustion Dynamics in a Multi-Element LOx–Methane Combustor Using Flamelet-Generated Manifold Approach," *Physics of Fluids*, Vol. 35, No. 11, 2023, Paper 115125.
https://doi.org/10.1063/5.0172100

[28] Li, G., Shi, B., Wang, N., Li, Q., and Zhao, M., "Supercritical Combustion Instabilities of Oxygen/Kerosene Mixture in a Swirl Coaxial Injector," *Applied Thermal Engineering*, Vol. 241, 2024, Paper 122429.
https://doi.org/10.1016/j.applthermaleng.2024.122429

[29] Sharma, A., De, A., and Kumar, S., "Investigation of Injector-Coupled Combustion Dynamics in a Methane-Oxygen Combustor Using Large

Eddy Simulation and Dynamic Mode Decomposition," *Physics of Fluids*, Vol. 36, No. 6, 2024, Paper 065116. https://doi.org/10.1063/5.0212604

[30] Huang, Y., Sung, H. G., Hsieh, S.-Y., and Yang, V., "Large-Eddy Simulation of Combustion Dynamics of Lean-Premixed Swirl-Stabilized Combustor," *Journal of Propulsion and Power*, Vol. 19, No. 5, 2003, pp. 782–794. https://doi.org/10.2514/2.6194

[31] Huang, Y., Wang, S., and Yang, V., "Systematic Analysis of Lean-Premixed Swirl-Stabilized Combustion," *AIAA Journal*, Vol. 44, No. 4, 2006, pp. 724–740. https://doi.org/10.2514/1.15382

[32] Zellhuber, M., Meraner, C., Kulkarni, R., Polifke, W., and Schuermans, B., "Large Eddy Simulation of Flame Response to Transverse Acoustic Excitation in a Model Reheat Combustor," *Journal of Engineering for Gas Turbines and Power*, Vol. 135, No. 9, 2013, Paper 091508. https://doi.org/10.1115/1.4024940

[33] Zellhuber, M., Schwing, J., Schuermans, B., Sattelmayer, T., and Polifke, W., "Experimental and Numerical Investigation of Thermoacoustic Sources Related to High-Frequency Instabilities," *International Journal of Spray and Combustion Dynamics*, Vol. 6, No. 1, 2014, pp. 1–34. https://doi.org/10.1260/1756-8277.6.1.1

[34] Huang, C., Gejji, R. M., Anderson, W. E., Yoon, C., and Sankaran, V., "Combustion Dynamics Behavior in a Single-Element Lean Direct Injection (LDI) Gas Turbine Combustor," *Proceedings of the 50th AIAA/ASME/SAE/ASEE Joint Propulsion Conference*, AIAA Paper 2014-3433, 2014. https://doi.org/10.2514/6.2014-3433

[35] Huang, C., Yoon, C., Gejji, R. M., Anderson, W., and Sankaran, V., "Computational Study of Combustion Dynamics in a Single-Element Lean Direct Injection Gas Turbine Combustor," *Proceedings of the 52nd Aerospace Sciences Meeting*, AIAA Paper 2014-0620, 2014. https://doi.org/10.2514/6.2014-0620

[36] Ghani, A., Poinsot, T., Gicquel, L., and Staffelbach, G., "LES of Longitudinal and Transverse Self-Excited Combustion Instabilities in a Bluff-Body Stabilized Turbulent Premixed Flame," *Combustion and Flame*, Vol. 162, No. 11, 2015, pp. 4075–4083. https://doi.org/10.1016/j.combustflame.2015.08.024

[37] Grimm, F., Lourier, J., Lammel, O., Noll, B., and Aigner, M., "A Selective Fast Fourier Filtering Approach Applied to Highfrequency Thermoacoustic Instability Analysis," *Proceedings of ASME Turbo Expo*, Paper GT2017-63234, 2017. https://doi.org/10.1115/GT2017-63234

[38] Sharifi, V., Beck, C., Janus, B., and Kempf, A., "Design and Testing of a High Frequency Thermoacoustic Combustion Experiment," *AIAA Journal*, Vol. 59, 2021, pp. 3127–3143. https://doi.org/10.2514/1.J060072

[39] Jella, S., Füri, M., and Katsapis, V., "Numerical Analysis of High Frequency Transverse Instabilities in a Can-Type Combustor," *Proceedings of ASME Turbo Expo*, Paper GT2023-103298, 2023. https://doi.org/10.1115/GT2023-103298

[40] Bonnaire, P., and Polifke, W., "Analysis of High-Frequency Dynamics of a Reacting Jet in Crossflow Based on Large Eddy Simulation," *Journal of Engineering for Gas Turbines and Power*, Vol. 146, No. 3, 2023, Paper 031002. https://doi.org/10.1115/1.4063540

[41] Kroniger, D., Kamiya, H., Horikawa, A., Suzuki, R., Munktell, E., and Braun, R., "LES and POD/DMD Analysis of Thermoacoustic Oscillation of a Hydrogen Micromix Flame Pair," *Proceedings of ASME Turbo Expo*, Paper GT2024-123589, 2024. https://doi.org/10.1115/GT2024-123589

[42] Krebs, W., Schulz, A., Witzel, B., Johnson, C., Laster, W., Pent, J., Schilp, R., Wasif, S., and Weaver, A., "Advanced Combustion System for High Efficiency (ACE) of the New SGT5/6-9000HL Gas Turbine," *Proceedings of ASME Turbo Expo*, Paper GT2022-82299, 2022. https://doi.org/10.1115/GT2022-82299

[43] Lumley, J. L., "The Structure of Inhomogeneous Turbulent Flows," *Atmospheric Turbulence and Radio Wave Propagation, Doklady Akademii Nauk SSSR*, Nauka, Moscow, 1967, pp. 166–177.

[44] Sirovich, L., "Turbulence and Dynamics of Coherent Structures. Part I: Coherent Structures," *Quarterly of Applied Mathematics*, Vol. 45, No. 3, 1987, pp. 561–571. https://doi.org/10.1090/qam/910462

[45] Rowley, C. W., Mezic, I., Bagheri, S., Schlatter, P., and Henningson, D. S., "Spectral Analysis of Nonlinear Flows," *Journal of Fluid Mechanics*, Vol. 641, 2009, pp. 115–127. https://doi.org/10.1017/S0022112009992059

[46] Schmid, P. J., "Dynamic Mode Decomposition of Numerical and Experimental Data," *Journal of Fluid Mechanics*, Vol. 656, 2010, pp. 5–28. https://doi.org/10.1017/S0022112010001217

[47] Taira, K., Brunton, S. L., Dawson, S. T. M., Rowley, C. W., Colonius, T., McKeon, B. J., Schmidt, O. T., Gordeyev, S., Theofilis, V., and Ukeiley, L. S., "Modal Analysis of Fluid Flows: An Overview," *AIAA Journal*, Vol. 55, No. 12, 2017, pp. 4013–4041. https://doi.org/10.2514/1.J056060

[48] Long, Y., Guo, X., and Xiao, T., "Research, Application and Future Prospect of Mode Decomposition in Fluid Mechanics," *Symmetry*, Vol. 16, No. 155, 2024, pp. 1–22. https://doi.org/10.3390/sym16020155

[49] Son, M., Armbruster, W., Tonti, F., and Hardi, J., "Numerical Study of Acoustic Resonance in a LOX Injector Post Induced by Orifice Flow," *AIAA Propulsion and Energy*, AIAA Paper 2021-3568, 2021. https://doi.org/10.2514/6.2021-3568

[50] Huang, C., Anderson, W. E., Harvazinski, M. E., and Sankaran, V., "Analysis of Self-Excited Combustion Instabilities Using Decomposition Techniques," *AIAA Journal*, Vol. 54, No. 9, 2016, pp. 2791–2807. https://doi.org/10.2514/1.J054557

[51] Yin, Z., and Stöhr, M., "Time-Frequency Localisation of Intermittent Dynamics in a Bistable Turbulent Swirl Flame," *Journal of Fluid Mechanics*, Vol. 882, 2020, Paper A30. https://doi.org/10.1017/jfm.2019.762

[52] Grader, M., Yin, Z., Geigle, K. P., and Gerlinger, P., "Influence of Flow Field Dynamics on Soot Evolution in an Aero-Engine Model Combustor," *Proceedings of the Combustion Institute*, Vol. 38, No. 4, 2021, pp. 6421–6429. https://doi.org/10.1016/j.proci.2020.05.019

[53] Lammel, O., Schütz, H., Schmitz, G., Lückerath, R., Stöhr, M., Noll, B., Aigner, M., Hase, M., and Krebs, W., "FLOX® Combustion at High Power Density and High Flame Temperatures," *Journal of Engineering for Gas Turbines and Power*, Vol. 132, No. 12, 2010, Paper 121503. https://doi.org/10.1115/1.4001825

[54] Fiolitakis, A., Lückerath, R., Lammel, O., Schmitz, G., Ax, H., Stöhr, M., Arndt, C., Noll, B., and Kluß, D., "Assessment of a Finite-Rate-Chemistry Model for ANSYS® CFX® Using Experimental Data of a Downsized Gas Turbine Combustor," *Proceedings of the ASME Turbo Expo*, Paper GT2018-75638, 2018. https://doi.org/10.1115/GT2018-75638

[55] Fleck, J., Griebel, P., Steinberg, A., Stöhr, M., Aigner, M., and Ciani, A., "Experimental Investigation of a Generic, Fuel Flexible Reheat Combustor at Gas Turbine Relevant Operating Conditions," *Proceedings of the ASME Turbo Expo*, Paper GT2010-22722, 2010, pp. 583–592. https://doi.org/10.1115/GT2010-22722

[56] Ax, H., Stopper, U., Meier, W., Aigner, M., and Güthe, F., "Experimental Analysis of the Combustion Behavior of a Gas Turbine Burner by Laser Measurement Techniques," *Journal of Engineering for Gas Turbines and Power*, Vol. 132, No. 5, 2010, Paper 051503. https://doi.org/10.1115/1.3205033

[57] Lückerath, R., Lammel, O., Stöhr, M., Boxx, I., Stopper, U., Meier, W., Janus, B., and Wegner, B., "Experimental Investigations of Flame Stabilization of a Gas Turbine Combustor," *Proceedings of the ASME Turbo Expo*, Paper GT2011-45790, 2011, pp. 725–736. https://doi.org/10.1115/GT2011-45790

[58] Lammel, O., Severin, M., Ax, H., Lückerath, R., Tomasello, A., Emmi, Y., Noll, B., Aigner, M., and Panek, L., "High Momentum Jet Flames at Elevated Pressure, A: Experimental and Numerical Investigation for Different Fuels," *Proceedings of the ASME Turbo Expo*, Paper GT2017-64615, 2017. https://doi.org/10.1115/GT2017-64615

[59] Fiolitakis, A., Pries, M., Lammel, O., and Kathrotia, T., "Investigation of High-Frequency Thermoacoustic Instabilities in a FLOX® Burner Using Large-Eddy Simulation and Multi Resolution Proper Orthogonal Decomposition," *Proceedings of the AIAA SCITECH*, AIAA Paper 2024-0794, 2024. https://doi.org/10.2514/6.2024-0794

[60] McBride, J., Gordon, S., and Reno, M., "Coefficients for Calculating Thermodynamic and Transport Properties of Individual Species," Tech. Rept. NASA TM 4513, NASA Lewis Research Center, Cleveland, OH, 1993.

[61] Fiolitakis, A., and Pries, M., "A Novel Approach to the Characteristic Splitting Scheme for Mildly Compressible Flows Based on the Weighted Averaged Flux Method," *Journal of Computational Physics*, Vol. 513, 2024, Paper 113197. https://doi.org/10.1016/j.jcp.2024.113197

[62] Pries, M., Fiolitakis, A., and Gerlinger, P., "An Implicit Splitting Scheme with Characteristic Boundary Conditions for Compressible Reactive Flows on Unstructured Grids," *Journal of Computational and Applied Mathematics*, Vol. 437, 2024, Paper 115446. https://doi.org/10.1016/j.cam.2023.115446

[63] Nicoud, F., and Ducros, F., "Subgrid-Scale Stress Modelling Based on the Square of the Velocity Gradient Tensor," *Flow, Turbulence and Combustion*, Vol. 62, No. 3, 1999, pp. 183–200. https://doi.org/10.1023/A:1009995426001

[64] Poinsot, T., and Veynante, D., *Theoretical and Numerical Combustion*, Aquaprint, Bordeaux, France, 2012, p. 173.

[65] Erlebacher, G., Hussaini, M. Y., Speziale, C. G., and Zang, T. A., "Toward the Large-Eddy Simulation of Compressible Turbulent Flows," *Journal of Fluid Mechanics*, Vol. 238, 1992, pp. 155–185. https://doi.org/10.1017/S0022112092001678

[66] De Vanna, F., Baldan, G., Picano, F., and Benini, E., "On the Coupling Between Wall-Modeled LES and Immersed Boundary Method Towards Applicative Compressible Flow Simulations," *Computers & Fluids*, Vol. 266, 2023, Paper 106058. https://doi.org/10.1016/j.compfluid.2023.106058

[67] Gerlinger, P., Möbus, H., and Brüggemann, D., "An Implicit Multigrid Method for Turbulent Combustion," *Journal of Computational Physics*, Vol. 167, No. 2, 2001, pp. 247–276. https://doi.org/10.1006/jcph.2000.6671

[68] Gerlinger, P., "Investigation of an Assumed PDF Approach for Finite-Rate Chemistry," *Combustion Science and Technology*, Vol. 175, No. 5, 2003, pp. 841–872. https://doi.org/10.1080/00102200302410

[69] Colin, O., Ducros, F., Veynante, D., and Poinsot, T., "A Thickened Flame Model for Large Eddy Simulations of Turbulent Premixed Combustion," *Physics of Fluids*, Vol. 12, No. 7, 2000, pp. 1843–1863. https://doi.org/10.1063/1.870436

[70] Charlette, F., Meneveau, C., and Veynante, D., "A Power-Law Flame Wrinkling Model for LES of Premixed Turbulent Combustion Part I: Non-Dynamic Formulation and Initial Tests," *Combustion and Flame*, Vol. 131, Nos. 1–2, 2002, pp. 159–180. https://doi.org/10.1016/S0010-2180(02)00400-5

[71] Poinsot, T., and Lele, S., "Boundary Conditions for Direct Simulations of Compressible Viscous Flows," *Journal of Computational Physics*, Vol. 101, No. 1, 1992, pp. 104–129. https://doi.org/10.1016/0021-9991(92)90046-2

[72] Yoo, C., Wang, Y., Trouve, A., and Im, H., "Characteristic Boundary Conditions for Direct Simulations of Turbulent Counterflow Flames," *Combustion Theory and Modelling*, Vol. 9, No. 4, 2005, pp. 617–646. https://doi.org/10.1080/13647830500307378

[73] Rudy, D., and Strikwerda, J., "A Nonreflecting Outflow Boundary Condition for Subsonic Navier-Stokes Calculations," *Journal of Computational Physics*, Vol. 36, No. 1, 1980, pp. 55–70. https://doi.org/10.1016/0021-9991(80)90174-6

[74] Kathrotia, T., Oßwald, P., Naumann, C., Richter, S., and Köhler, M., "Combustion Kinetics of Alternative Jet Fuels, Part-II: Reaction Model for Fuel Surrogate," *Fuel*, Vol. 302, 2021, Paper 120736. https://doi.org/10.1016/j.fuel.2021.120736

[75] Grader, M., and Gerlinger, P., "Influence of Operating Conditions on Flow Field Dynamics and Soot Formation in an Aero-Engine Model Combustor," *Combustion and Flame*, Vol. 258, 2023, Paper 112712. https://doi.org/10.1016/j.combustflame.2023.112712

[76] Stöhr, M., Sadanandan, R., and Meier, W., "Phase-Resolved Characterization of Vortex-Flame Interaction in a Turbulent Swirl Flame," *Experiments in Fluids*, Vol. 51, No. 4, 2011, pp. 1153–1167. https://doi.org/10.1007/s00348-011-1134-y

[77] Daubechies, I., *Ten Lectures on Wavelets*, Soc. for Industrial and Applied Mathematics, Philadelphia, Pennsylvania, 1992. https://doi.org/10.1137/1.9781611970104

[78] Percival, D. B., and Walden, A. T., *Wavelet Methods for Time Series Analysis*, Cambridge Univ. Press, Cambridge, 2006, p. 112.

[79] Upatnieks, A., Driscoll, J., and Ceccio, S., "Cinema Particle Imaging Velocimetry Time History of the Propagation Velocity of the Base of a Lifted Turbulent Jet Flame," *Proceedings of the Combustion Institute*, Vol. 29, No. 2, 2002, pp. 1897–1903. https://doi.org/10.1016/S1540-7489(02)80230-9

[80] Peters, N., *Turbulent Combustion, Cambridge Monographs on Mechanics*, Cambridge Univ. Press, Cambridge, 2004, p. 175. https://doi.org/10.1017/CBO9780511612701

[81] Rütten, F., Schröder, W., and Meinke, M., "Large-Eddy Simulation of Low Frequency Oscillations of the Dean Vortices in Turbulent Pipe Bend Flows," *Physics of Fluids*, Vol. 17, No. 3, 2005, Paper 035107. https://doi.org/10.1063/1.1852573

[82] Lupi, V., Canton, J., and Schlatter, P., "Global Stability Analysis of a 90°-Bend Pipe Flow," *International Journal of Heat and Fluid Flow*, Vol. 86, 2020, Paper 108742. https://doi.org/10.1016/j.ijheatfluidflow.2020.108742

[83] Coats, C., "Coherent Structures in Combustion," *Progress in Energy and Combustion Science*, Vol. 22, No. 5, 1996, pp. 427–509. https://doi.org/10.1016/S0360-1285(96)00011-1

[84] Clanet, C., Searby, G., and Clavin, P., "Primary Acoustic Instability of Flames Propagating in Tubes: Cases of Spray and Premixed Gas Combustion," *Journal of Fluid Mechanics*, Vol. 385, 1999, pp. 157–197. https://doi.org/10.1017/S0022112099004231

[85] Goodwin, D. G., Moffat, H. K., Schoegl, I., Speth, R. L., and Weber, B. W., "Cantera: An Object-Oriented Software Toolkit for Chemical Kinetics, Thermodynamics, and Transport Processes," May 2022. https://doi.org/10.5281/zenodo.6387882

[86] Beardsell, G., and Blanquart, G., "Impact of Pressure Fluctuations on the Dynamics of Laminar Premixed Flames," *Proceedings of the Combustion Institute*, Vol. 37, No. 2, 2019, pp. 1895–1902. https://doi.org/10.1016/j.proci.2018.07.125

J. C. Oefelein
Associate Editor